2021-06

SURFACE VESSEL ACOUSTIC SIGNAL DIRECTION OF ARRIVAL ESTIMATION BY VECTOR SENSOR PROCESSING WITH THE MAXIMUM EIGENGAP ESTIMATOR

Foster, Jacob W.

Monterey, CA; Naval Postgraduate School

NAVAL POSTGRADUATE SCHOOL

MONTEREY, CALIFORNIA

THESIS

SURFACE VESSEL ACOUSTIC SIGNAL DIRECTION OF ARRIVAL ESTIMATION BY VECTOR SENSOR PROCESSING WITH THE MAXIMUM EIGENGAP ESTIMATOR

by

Jacob W. Foster

June 2021

Thesis Advisor:	Robert L. Bassett
Co-Advisor:	Paul Leary
Second Reader:	Kay L. Gemba, U.S. Naval Research Laboratory

THIS PAGE INTENTIONALLY LEFT BLANK

REPORT DOCUMENTATION PAGE			*Form Approved OMB No. 0704-0188*

1. AGENCY USE ONLY *(Leave blank)*	**2. REPORT DATE** June 2021	**3. REPORT TYPE AND DATES COVERED** Master's thesis

4. TITLE AND SUBTITLE
SURFACE VESSEL ACOUSTIC SIGNAL DIRECTION OF ARRIVAL ESTIMATION BY VECTOR SENSOR PROCESSING WITH THE MAXIMUM EIGENGAP ESTIMATOR

5. FUNDING NUMBERS

6. AUTHOR(S) Jacob W. Foster

7. PERFORMING ORGANIZATION NAME(S) AND ADDRESS(ES)
Naval Postgraduate School
Monterey, CA 93943-5000

8. PERFORMING ORGANIZATION REPORT NUMBER

9. SPONSORING / MONITORING AGENCY NAME(S) AND ADDRESS(ES)
N/A

10. SPONSORING / MONITORING AGENCY REPORT NUMBER

11. SUPPLEMENTARY NOTES The views expressed in this thesis are those of the author and do not reflect the official policy or position of the Department of Defense or the U.S. Government.

12a. DISTRIBUTION / AVAILABILITY STATEMENT
Approved for public release. Distribution is unlimited.

12b. DISTRIBUTION CODE
A

13. ABSTRACT (maximum 200 words)

This work intends to improve Navy/Marine Corps reconnaissance capabilities for operations in near-shore–contested amphibious environments. We present a novel unsupervised approach to vessel localization, the maximum eigengap estimator, by analyzing the multi-directional signal channels from a single vector sensor connected to the cabled observatory operated by the Monterey Bay Aquarium Research Institute–Monterey Accelerated Research System (MBARI-MARS). This work postulates that the direction of arrival and frequency of a vessel source signal can be identified by optimizing the weights over the aggregated cross-power spectral density matrices of a vector sensor's directional channels. We explore the accuracy of the maximum eigengap estimator's performance with various upper and lower bounds for frequency selection, and by changing source distance and direction to the sensor, and against multi-source scenarios. The estimator shows agreement with the physics-informed Bellhop ray model and produces accurate estimations for direction of arrival for single source estimations within a 12-kilometer range from the sensor. We also demonstrate the novelty of the algorithm to produce automatic selection of source frequency.

14. SUBJECT TERMS
hydrophone, localization, machine learning, underwater acoustics, covariance matrix, tensor decomposition, vector sensor

15. NUMBER OF PAGES
67

16. PRICE CODE

17. SECURITY CLASSIFICATION OF REPORT	**18. SECURITY CLASSIFICATION OF THIS PAGE**	**19. SECURITY CLASSIFICATION OF ABSTRACT**	**20. LIMITATION OF ABSTRACT**
Unclassified	Unclassified	Unclassified	UU

NSN 7540-01-280-5500

Standard Form 298 (Rev. 2-89)
Prescribed by ANSI Std. 239-18

THIS PAGE INTENTIONALLY LEFT BLANK

Approved for public release. Distribution is unlimited.

SURFACE VESSEL ACOUSTIC SIGNAL DIRECTION OF ARRIVAL ESTIMATION BY VECTOR SENSOR PROCESSING WITH THE MAXIMUM EIGENGAP ESTIMATOR

Jacob W. Foster
Captain, United States Marine Corps
BS, Texas A & M University, 2009

Submitted in partial fulfillment of the
requirements for the degree of

MASTER OF SCIENCE IN OPERATIONS RESEARCH

from the

NAVAL POSTGRADUATE SCHOOL
June 2021

Approved by: Robert L. Bassett
Advisor

Paul Leary
Co-Advisor

Kay L. Gemba
Second Reader

W. Matthew Carlyle
Chair, Department of Operations Research

THIS PAGE INTENTIONALLY LEFT BLANK

ABSTRACT

This work intends to improve Navy/Marine Corps reconnaissance capabilities for operations in near-shore–contested amphibious environments. We present a novel unsupervised approach to vessel localization, the maximum eigengap estimator, by analyzing the multi-directional signal channels from a single vector sensor connected to the cabled observatory operated by the Monterey Bay Aquarium Research Institute–Monterey Accelerated Research System (MBARI-MARS). This work postulates that the direction of arrival and frequency of a vessel source signal can be identified by optimizing the weights over the aggregated cross-power spectral density matrices of a vector sensor's directional channels. We explore the accuracy of the maximum eigengap estimator's performance with various upper and lower bounds for frequency selection, and by changing source distance and direction to the sensor, and against multi-source scenarios. The estimator shows agreement with the physics-informed Bellhop ray model and produces accurate estimations for direction of arrival for single source estimations within a 12-kilometer range from the sensor. We also demonstrate the novelty of the algorithm to produce automatic selection of source frequency.

THIS PAGE INTENTIONALLY LEFT BLANK

Table of Contents

THIS PAGE INTENTIONALLY LEFT BLANK

List of Figures

THIS PAGE INTENTIONALLY LEFT BLANK

List of Tables

THIS PAGE INTENTIONALLY LEFT BLANK

List of Acronyms and Abbreviations

AI	Artificial Intelligence
AIS	Automatic Identification System
CSD	Cross Spectral Density
CNN	Convolutional Neural Network
DOA	Direction of Arrival
DoD	Department of Defense
EABO	Expeditionary Advanced Base Operations
GPS	Global Positioning System
HPC	High Performance Computer
KNN	K-Nearest Neighbors
MAAD	Mean Absolute Angular Deviation
MARS	Monterey Accelerated Research System
MBARI	Monterey Bay Aquarium Research Institute
MMSI	Maritime Mobile Service Identity
ML	Machine Learning
NN	Neural Network
NPS	Naval Postgraduate School
SNR	Signal to Noise Ratio
SOI	Source of Interest

SOSUS Sound Ocean Surveillance System

TDNN Time-Delay Neural Network

USCG United States Coast Guard

USN United States Navy

USMC United States Marine Corps

UUV Unmanned Underwater Vehicle

Executive Summary

This thesis presents the maximum eigengap estimator as a novel passive acoustic localization algorithm. The algorithm is applied to data from a vector sensor hydrophone located in the sub-marine Monterey Canyon off the coast of Monterey, California. We use vessel Global Positioning System data, provided by the US Coast Guard in the form of Automatic Identification System data, to compute the bearings and validate the estimator's performance. The main purpose of this thesis is to answer the question: how well does the maximum eigengap estimator perform for vessel localization using empirical data from a vector sensor?

First we discuss the military context, and research background in acoustic localization. Then we cover the data used in this thesis, and we provide a brief explanation on the basics of acoustic propagation in the ocean environment. We show the results of an acoustic propagation model to provide a physics informed baseline for the expected performance of the maximum eigengap estimator. After discussing the derivation and implementation, we present the results of experiments that explore the performance of the estimator for acoustic sources at various distances and directions. Also, we analyze the effect of multiple signals in the acoustic record, and determine that closer vessels generally produce better estimates (within 10 km from the sensor). The maximum eigengap estimator also shows relatively good results for vessels in oceanographic areas where, in agreement with the an acoustic propagation model, the bathymetry does not impede the acoustic path. We also see the maximum eigengap estimator is able to produce accurate estimates at further distances when we narrow the frequency selection range to 75 to 100 Hz. Lastly, we show the advantage the algorithm has when we produce bearing estimates for a large data set over a wide oceanographic area to generate a map of vessel localization estimate error.

Recommendations for future work include expanding the analysis to computing the estimator's performance under various deployment conditions and environments. Significant insights may be gained by understanding the effects of seasonally changing temperatures in the water column, various sea floor and bathymetric characteristics, and alternate sensor placement depths.

THIS PAGE INTENTIONALLY LEFT BLANK

Acknowledgments

I owe an immense deal of gratitude to Dr. Bassett for his dedication and leadership in this project. I am in debt for all of the time and effort he has offered in patiently mentoring me along the way. Thank you to Dr. Leary, and Dr. Gemba for all of the contributions they have made to provide the in-depth acoustics expertise that has uniquely enhanced my education while at the Naval Postgraduate School. I want to thank the outstanding faculty in the Operations Research department for cultivating a culture of excellence within the student body.

Special appreciation goes to my parents for their love, support, and for the opportunities they have built for me. Thank you to my brother Joshua, who has challenged me and pushed me to be better, and to my sisters Kari and Kylie, who have given me something to fight for. For all of my brothers and sisters in arms, thank you for your service, sacrifice, and for making me want to be a better officer. And lastly, my deepest thanks go to my grandmother Jimmie Sue Browning, this thesis is in memory of your kind heart.

THIS PAGE INTENTIONALLY LEFT BLANK

CHAPTER 1:
Introduction

Acoustic analysis from hydrophones has been a mainstay in detection technologies since the dawn of undersea warfare and sonar. Sonar technology grew out of a Naval need for surface vessels to locate lurking enemy submarines. There are many different methods and technologies that are used to conduct undersea acoustic analysis. This thesis explores the use of a novel algorithm that is applied to a hydrophone to conduct localization of a surface vessel. Localization, in this sense, refers to the process of using the noise that is generated by a vessel (i.e. by its propeller, or the rumble of machinery transmitted through the hull, etc.), and is received by the vector sensor to find the vessel's location. The hydrophone that is used in this research is a vector sensor which receives directional sound measurements from velocity and pressure sensors in the device.

Applications of passive acoustic technologies enable users to detect sound sources (vessels, marine mammals, geologic events) without emitting any sound signals. In the military context this means that forces can identify enemy vessels without giving away their position or yielding any knowledge to the enemy that there is a detection technology present. The United States Navy employs hydrophone sensors for this purpose though it often requires human analysis of the gathered data. In this chapter the problem statement, applicability and military relevance are presented. We also give a brief review of the relevant literature.

1.1 Problem Statement

This thesis presents a novel algorithm to localize the source of an ocean acoustic signal. The algorithm we present (the maximum eigengap estimator) leverages information from the velocity channels of a single acoustic vector sensor, and is a data-driven approach to localization. In contrast, traditional methods of localization require physics-informed acoustic models of the ocean environment and some level of human interpretation of the analytical results of those models. This human interpretation requires significant multi-disciplinary training and expertise in the fields of ocean acoustics and signals processing. By automating signal source localization, the algorithm removes the human from the loop

of the localization process and source signal frequency selection, increasing the speed and scale of analysis. This contribution has many potential applications in both military and scientific contexts. Furthermore, integration of the algorithm into operational sensors may provide near instantaneous real time bearing detection capabilities. The question we attempt to answer in this thesis is: how does the maximum eigengap estimator perform for vessel localization using empirical data from an acoustic vector sensor?

1.2 Military Relevance

Since vessel detection requires post-processing and human analysis of the received acoustic signal there is a need for reducing the analysis workload of soldiers and sailors who fill the high demand, low density occupational specialties as sonar analysts. Furthermore, modern advancements in artificial intelligence (AI) have prompted the DoD to employ AI-driven systems to automate sensor technologies and improve the speed of operational capabilities. Leveraging artificially intelligent acoustic analysis removes the human from the loop of acoustic sensor analysis and provides more flexibility to the warfighter to accomplish other tasks. At the same time, AI sensor systems improve the speed of localization and the scale at which the data is analyzed.

Specific implications for AI-driven hydrophone sensors also complement the current force-design promulgated by the Commandant of the Marine Corps in the 38th Commandant's Planning Guidance (Berger 2020). The United States Marine Corps (USMC) is undertaking a "Shift to the Pacific" and conducting restructuring and force design focused on supporting the US Navy's mission set and countering peer-adversarial threats among the island chains of the South China Sea. This shift has garnered interest in combining the capabilities provided by AI and acoustic sensor technologies, and amphibious Marine forces to conduct Naval combat support operations.

In the Expeditionary Advanced Base Operations (EABO) context, small unit forces are expected to be distributed over great distances and operate autonomously from parent commands. Marine forces in support of Naval operations will need to be connected to higher-level sensor networks and will require the ability to observe, detect, and target enemy surface and subsurface vessels. As the demand for acoustic localization increases, the supply of trained technicians to monitor the acoustic network diminishes. AI acoustic

vessel localization will enable Marine forces to be seamlessly integrated into the sensor network without taxing the manpower requirement of sensor analysts.

The application of AI-driven localization also improves the scale at which it can occur. In traditional methods, the hydrophone signal is sent to an analyst who analyzes the signal. With an AI acoustic sensor the scale of analysis is virtually limitless. In the AI setting, the scale of samples that can be analyzed is as large as the number of computer nodes assigned the problem, and analysis occurs at the speed of electrons in the microprocessors. The implications for this scaling are that relatively cheaply procured sensors can be deployed across swaths of oceanographic areas of interest, and autonomously monitored, so that directional information of enemy ships is provided directly from the sensors to the warfighter.

1.3 Literature Review

The literature on the field of ocean acoustics has a long history and is wide and deep in subject areas. One of the larger subject areas is hydro-acoustic direction of arrival (DOA) estimation using measurements from arrays of hydrophones each receiving an omni-directional pressure signal. Vector sensors are unique from other hydrophones in that the received acoustic signal contains the traditional omni-directional acoustic pressure signal channel, and in addition includes channels providing acoustic particle velocity measurements along three orthogonal axes. The advantage of adding the velocity measurements is that this sensor offers more information about the acoustic environment in a smaller sensor system than conventional hydrophone arrays.

Early development of acoustic localization began during World Wars I and II. Development continued into the Cold War when detection of enemy submarines in coastal waters became a major national security interest in the United States (Rossing 2007). The US Navy invested heavily in the sound ocean surveillance system (SOSUS) network to counter Soviet submarine threats, and technological advancements from that legacy program continue to this day. The SOSUS network was built as an array of sensors distributed among submarine hilltops where they could detect enemy vessels and relay that information to shore.

In the late 1980's and early 1990's acoustic vector sensor technologies began to show promise as an upgrade to existing omnidirectional hydrophone arrays to determine the

DOA of an acoustic signal. Early work was introduced by Nehorai and Paldi (1994), who provided two algorithms to compute the direction-of-arrival (DOA) of the source to a vector sensor in the single and multi-source/sensor setting. Both algorithms assume that the acoustic signal arrives at the sensor as a plane wave, and the signal spectrum is band limited. The algorithms presented here utilize the eigenvectors from the covariance matrix and the statistical moments of the pressure and velocity channels. The solutions were derived from the assumption that the acoustic pressure, from a source in a given direction, is equal to the omni-directional pressure received at the sensor in that direction plus some noise. This is shown in equation (1.1) and presented as a time domain realization of the DOA problem where $y(t)$ is velocity measurement in the direction of u (after scaling). $P(t)$ is the omni-directional pressure measured by the sensor, u is the unit vector pointing from the sensor to the signal source, and $e(t)$ is the noise. This time domain formulation is attractive in its simplicity but does not discriminate signals by individual frequency.

$$y(t) = P(t)\, u + e(t) \tag{1.1}$$

Hawkes and Nehorai (1998) extended the covariance time domain approach to DOA estimation for arrays of acoustic vector sensors, demonstrating an increase in signal to noise ratio (SNR) and applicability of acoustic beamforming methods to determine both azimuth and elevation. Their work used Monte-Carlo simulations to validate the conclusion that an increase in the number of sensors in an array decreases directional sensitivity if the aperture is unbounded by distance. This result is particularly useful as a comparison to this thesis as we have only used measurements from a single vector sensor and provide a DOA estimator from two of the velocity channels.

More recently, Nichols et al. (2019) demonstrated the directional advantage that vector sensors have by improving the Green's function estimates against traditional omnidirectional hydrophones. The time domain Green's function (also known as the channel impulse response) in underwater acoustics is a description of the possible paths from the source to the sensor. While this thesis presents a novel frequency domain approach to determine DOA, the work of Nichols et al. (2019) indicates the promising future and applicability of vector sensors to real world data from their Long Island Sound experiments.

Adjacent work on acoustic DOA estimation has been abundantly published in the signals

processing literature. In the passive acoustic setting, noise signals in the ocean arrive from various sources which are unknown to the sensor or the observer. Figure 1.1 displays the various contributions of noise sources in the ocean and the frequencies they exhibit. Since the intent of this thesis is to provide an unsupervised DOA estimation from an unknown source, the problem inherently requires wide-band analysis and lends itself towards a frequency domain approach.

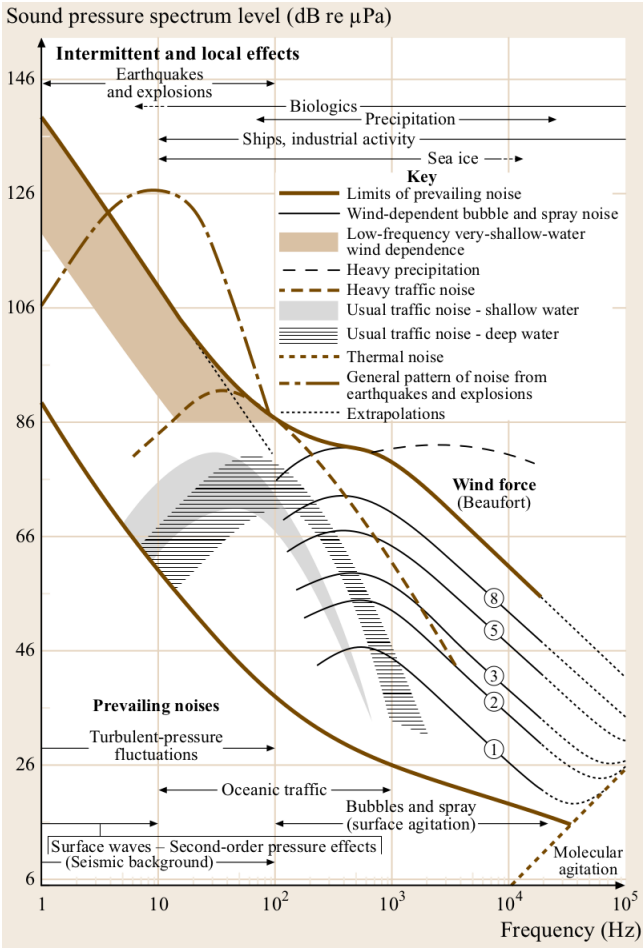

Figure 1.1. Spectral Density Levels of Common Ambient Noise Sources in the Ocean (Rossing 2007).

DOA estimates of a unique signal from a wide-band measurement can be found by combining the cross-spectral density (CSD) matrices across a frequency range to maximize the SNR of

the resulting signal subspace. Much of the work on DOA estimates in the frequency domain (referenced below) has been performed on the more common hydrophones which provide only information from the omni-directional pressure channel. Generally, the deconstruction of a wide-band signal in the frequency domain provides narrow-band information about each frequency in the form of the CSD matrix. After the CSD matrices are aggregated, the SNR and DOA estimates can be computed. Several different approaches have been presented on how this aggregation may be performed. Wang and Kaveh (1985) used a linear combination of the CSD matrices at each frequency, but applied an equal weighting of each matrix. Alternatively, Cadzow (1990) aggregated narrow-band frequency information using an approximating equation for the signal subspace, which is a linear combination of generalized eigenvector equations for each frequency. This thesis presents a DOA algorithm which also aggregates the narrow-band information from a wide-band signal, but we leverage the vector sensor's directional channels to optimize the SNR over the weights in a linear combination of cross-spectral power matrices. The details of this aggregation are discussed in Chapter 3.

It is important to note that the data used to validate the results in this thesis are entirely ocean signals from a vector sensor in the submarine Monterey Canyon. We have used ocean-going surface vessels as sources of opportunity in the vicinity of the Monterey Canyon to conduct our experiments and validate the DOA estimations. Experimental work using ships as sources of opportunity is relatively common in the ocean acoustic body of knowledge, and there are many promising future applications this work could extend to. The added benefit of using ships as sources of opportunity offers easily accessible sound sources for not only the purpose of testing novel DOA algorithms, but also for classifying the environment. Koch and Knobles (2005) used ships as sources of opportunity to conduct geo-acoustic inversion analysis on hydrophone data to classify the ocean bottom sediment layers in shallow water. Not only is classifying the ocean bathymetry and sediment layers important for understanding acoustic wave propagation and bottom reflections, but knowledge of the sediment layer is important for a wide range of military and civilian applications (from amphibious landing reconnaissance to offshore mineral and oil exploration). Gemba et al. (2018) used a matched filter beam-forming method on noise sources from surface vessels to determine the channel impulse response which was shown to contain information on the water column sound speed profile, seafloor depth, and sediment layers.

The process of using sources of opportunity in the passive acoustic setting, where the ship location is unknown a priori, draws quick comparisons to machine learning (ML) studies. The benefit to taking an ML approach to acoustic analysis is the absence of a physical acoustic model. In contrast, the data-first perspective is agnostic to many of the physical assumptions about the data or the acoustic environment. There have been several recent inroads into applying ML algorithms to ocean acoustic data and this thesis is a direct extension of one such application. Kim (2020) developed and applied a convolutional neural network (CNN) to data from the omni-directional channel of the same vector sensor as this thesis as an attempt to conduct vessel identification and classification in the spectogram. Several researchers have attempted other neural network approaches. Huang et al. (2018) employed a deep time-delay neural network (TDNN) on a wide variety of acoustic sources and settings and showed performance gains over traditional matched field processing results. Niu et al. (2017) used the sample covariance matrix of measurements from an acoustic vector sensor in a feed-forward neural network (NN) to predict source localization with favorable results.

This thesis presents a data driven approach to source localization by the maximum eigengap estimator that is more tractable and arguably more explainable than other ML methods. An additional novelty is that this algorithm relies on the x, and y channels of a vector sensor, rather than traditional omnidirectional hydrophones. We also present the results of a physical acoustic model and discuss the differences to the results of the maximum eigengap estimator. Chapter 2 is a discussion on the collection, characterization, and processing of the data used in this thesis. In Chapter 3 we provide the derivation for the maximum eigengap estimator, and present the results of the experiments using the algorithm. We show that the algorithm generally agrees with physics-based models for single source observations. In a companion paper we show the maximum eigengap estimator outperforms other traditional methods for bearing estimation using a vector sensor's velocity channels citepBassett.

THIS PAGE INTENTIONALLY LEFT BLANK

CHAPTER 2:
The Data and the Environment

The maximum eigengap estimator's performance was validated on data from several sources: the acoustic measurements from the vector sensor, and the empirical noise source locations from AIS data. The collection and processing of this data required collaborative efforts from multiple organizations. Researchers at the Monterey Bay Aquarium Research Institute (MBARI) and in the Department of Physics at NPS deployed and maintain the vector sensor. The acoustic data from the vector sensor is hosted on the NPS computer cluster and initial processing was performed by the NPS Physics Department. A year's worth of acoustic data (January - December 2019) was compiled into an SQLite database and hosted on the high-performance computer (HPC), Hamming. This work began as a continuation of prior NPS thesis work conducted by Kim (2020) who used the spectograms generated from the vector sensor's omni-directional channel and AIS data to train a convolutional neural network (CNN) in an attempt to detect the presence of a surface vessel's acoustic signature in the spectogram. An accompanying year's worth (January - December 2019) of AIS shipping data was provided by the United States Coast Guard (USCG) for a region around the vector sensor. This was also imported into an SQLite database and hosted on the HPC. Lastly, the Naval Research Lab provided results from a physical acoustic model for selected paths from the vector sensor.

2.1 Vector Sensor

A single Geospectrum M20-105 vector sensor is connected to the Monterey Accelerated Research System (MARS), a cabled observatory operated by the Monterey Bay Aquarium Research Institute (MBARI), located on the seafloor of the Monterey Canyon at 1000 meters water depth. The device has four measurement components: 3-orthogonal velocity sensors and an omnidirectional pressure sensor. As ocean acoustic waves pass by the sensor, pressure and velocity measurements are recorded as electric signals that are streamed from MARS directly to a server housed at NPS. According to the manufacturer, the lower limit of detection for the sensor is 10-20 Hz, and it has an upper limit near 1200-2000 Hz. The term "noise", as used in this document, refers to any perceived sound source other than the

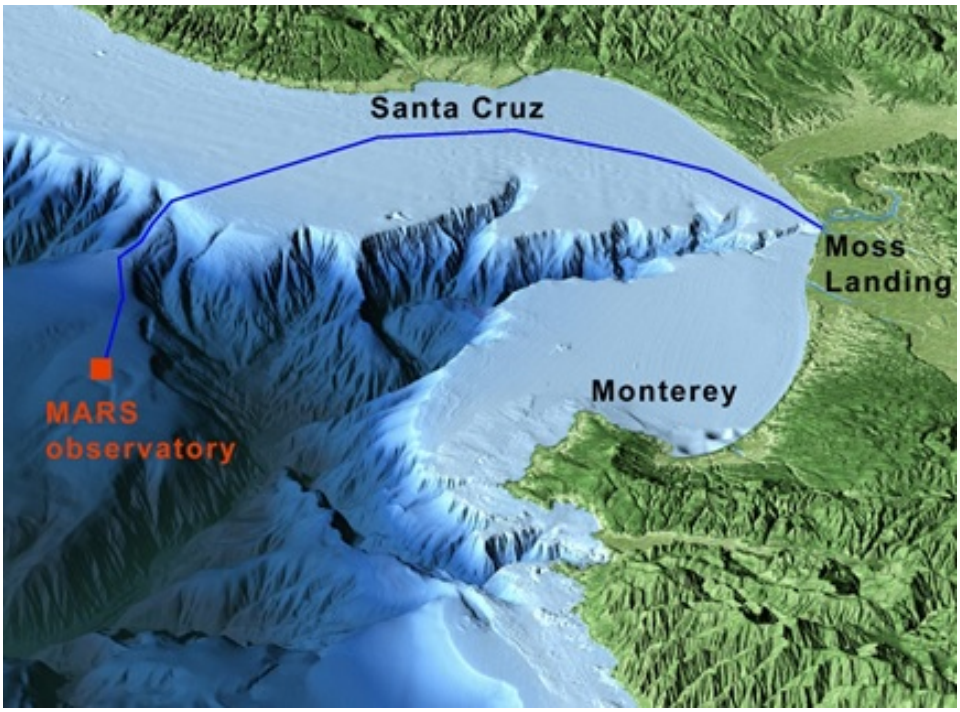

Figure 2.1. MARS Cabled Observatory, Vector Sensor Location in Monterey Canyon. Source: (Kuhnz et al. 2020).

vessel of interest and exists within the sensor's frequency detection range. Other common noise sources present in the data come from marine mammals, vessels, cavitation produced by surface waves, and seismic events.

The maximum eigengap estimator is a frequency domain algorithm that discriminates between noise sources in the data. The details of this discrimination is the novelty of this thesis and discussed in the next chapter. We consider both a calibrated and uncalibrated version of the data. For the calibrated data we applied a linear filter to the sound data in order to correct for the frequency response curve of the sensor's accelerometer and convert the velocity channels into pressure units. The uncalibrated data was left untransformed as collected from the sensor. The acoustic data also includes the vector sensor's orientation. The orientation error as provided by the manufacturer is less than 5 degrees relative to magnetic North. The azimuth of the sensor is oriented about 45 degrees North-East and a correction was made to align it to true North.

2.2 AIS Data

The AIS Data used in this study was provided by the United States Coast Guard. Each observation is unique to a single ship traveling over a five minute window in the region (geo coordinates) identified by the timestamp and ship maritime mobile service identity (MMSI). There are inconsistencies in several of the fields provided in the AIS data. Namely, many of the fields which provide vessel characteristic information are missing. The most consistent fields, and most useful for this study, are the GPS coordinates of the vessels. Table 2.1 describes the majority of the fields in the AIS data. Additional vessel dimensional fields are omitted from the table 2.1 for brevity. The latitude and longitude coordinates were used to compute the bearing from the sensor to the vessel in order to analyze the accuracy of the maximum eigengap estimator bearing predictions. The geodesic distance uses a more accurate ellipsoidal approximation (Hooijberg 2012) for the shape of the earth, rather than the Haversine spherical approximation, and was used to compute the bearing and distance. The maximum eigengap estimator was compared to these bearing computations after correction for magnetic declination. Vessels transmit AIS and location information every two to ten seconds and these are averaged. The 'PERIOD' field in the AIS data is a timestamp at the end of the 5 minute observation period that the data are averaged over. These timestamps are used to identify the acoustic data from the vector sensor with an appropriate five minute sample.

After storing the AIS data in an SQLite database, Python code was written to extract sets of individual observations of surface vessels by timestamp near the sensor based on their GPS coordinates. The largest geographic area that was used for maximum eigengap estimation error computation was a box between latitudes 36.392349 and 37.110651 decimal degrees and longitudes -122.186898 and -123.108576 decimal degrees. It should be noted that not every ship broadcasts its GPS coordinates via AIS, and GPS locations are prone to error depending on a multitude of factors (Rossing 2007).

The MMSI field proved useful to identify individual vessel tracks. There is some potential for future analysis if more data were available in the 'SHIP_AND_CARGO_TYPE' and 'DRAUGHT' since one would expect more energy in acoustic signals from larger ships. However, many of these fields were missing for unique vessel observations. Additionally, though the AIS data provides reasonable information about the truth of a sound source location there are many other factors which are not captured. It is known that MBARI

routinely performs maintenance on the MARS observatory and the vector sensor with an Unmanned Underwater Vehicle (UUV). The UUV generates noise near the sensor but does not broadcast an AIS signal. Also, the Monterey Canyon is home to many species of marine mammals, including whales that sing at frequencies near those in the surface vessel range that would produce errors in the maximum eigengap bearing estimates. Other sources of error may come from vessels that broadcast AIS positions, but do not emit noise, either while operating under sail power or moored at sea.

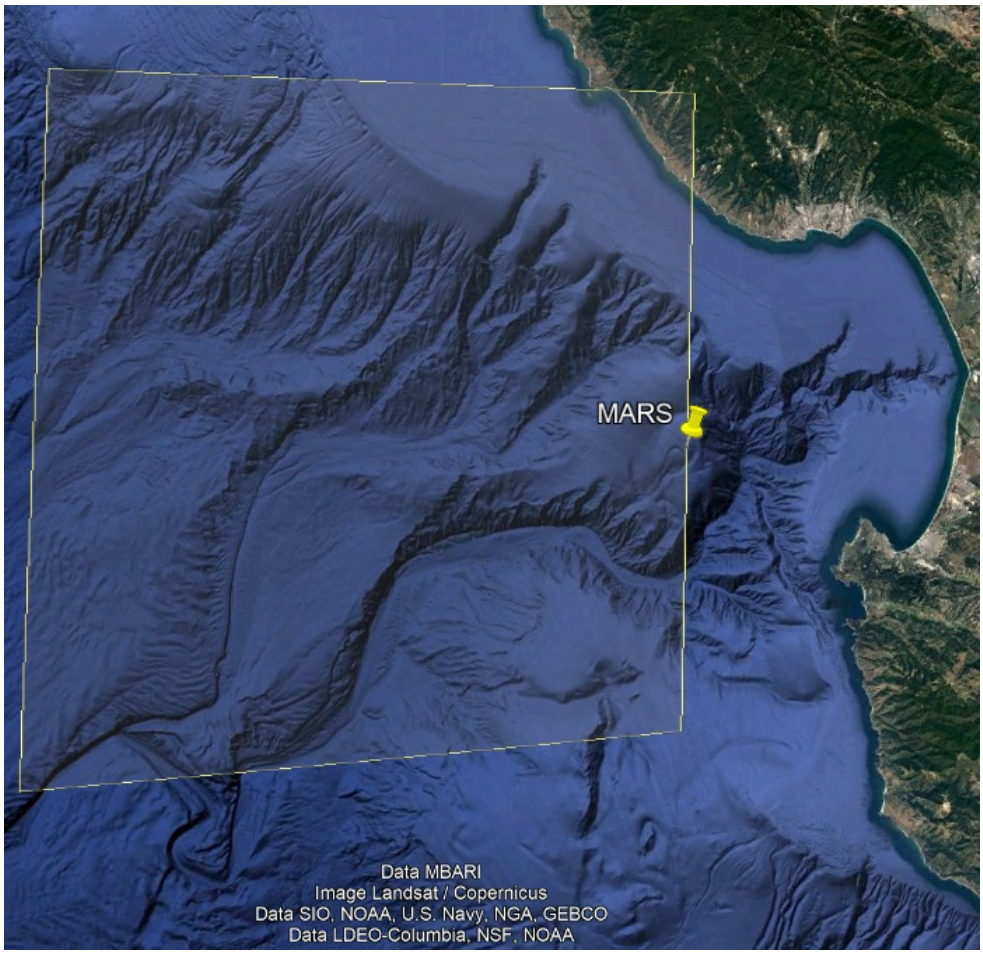

Figure 2.2. Area of AIS Observations.

Table 2.1. AIS Data Fields

Field Name	Long Name	Description	Data Type
MMSI	Maritime Mobile Service Identity	9 Digit Identifier	integer
NAME	—-	Vessel Name	text
IMO_NUMBER	International Maritime Organization number	7 digit unique vessel identifier	integer
CALL_SIGN	—-	Vessel Radio Call Sign	text
LAT_AVG	Latitude Average	vessel 5 minute average latitude	real
LON_AVG	Longitude Average	vessel 5 minute average longitude	real
PERIOD	—-	AIS 5 minute observation period	timestamp
SPEED_KNOTS	—-	Vessel speed	real
COG_DEG	Course over ground	heading relative to true north	real
NAV_STATUS	Navigation Status	“at anchor”, “under way using engines”	text
NAV_SENSOR	Navigation Sensor Location	Location of GPS sensor in meters aft of bow and meters port or starboard	int
SHIP_AND_CARGO_TYPE	—-	type of ship and cargo	integer
DRAUGHT	—-	vessel draught in meters	real
DIM_BOW	Bow dimensions	dimensions of the ships bow to nearest meter	integer
Destination	—-	Destination port of transit	text
BEARING	—-	true bearing at own position (0-359)	real
DIST	Distance	distance to nearest ship	real

2.3 Oceanographic Environment

Acoustic waves follow the path of least resistance towards the trough in the water column's sound speed profile. This is described by Snell's Law. An example sound speed profile is shown in 2.3. Since sound travels slower in lower density mediums, an acoustic wave front propagating through that medium will refract, or bend, towards the decreasing gradient in the sound speed profile of the water column. Thus, the path of an acoustic wave depends on the incident angle of approach and will continue bending upwards and downwards between conjugate refraction points in the sound speed profile. The resultant path of the acoustic wave yields loud or quiet zones in the ocean where observation of a noise source is available or diminished. As the weather changes year round, seasonal patterns of warming and cooling in the ocean drive changes in the sound speed profile as well as contributions from tidal, salinity, and temperature ocean water mixing. It has been shown that currents, tidal and freshwater exchanges are also present in the Monterey Canyon adding further complexity to the oceanographic environment (Carter and Gregg 2002) (Hollister September 1975).

Physics-informed acoustic models attempt to mathematically describe the physical process through differential equations as well some statistics based approaches (Etter 2018). In contrast, the data-driven approach, such as the one presented in this thesis as the maximum eigengap estimator, may be considered a naive statistical method. The analysis of an acoustic environment by physics-informed methods is limited by the assumptions required for the method.

An advantage to data-driven acoustic analyses is they do not share the same assumption bias that physics-informed methods do. This is because physics-informed models require detailed assumptions about the ocean environment and source characteristics (for example frequency, velocity, source level, etc). These assumptions will always be an approximation and different than the reality. The data-first approach we present does not require any assumptions about the environment and automatically determines the source frequency. Rather, the complexities that physics-informed models provide are already in the data, and the data analyst uses tools to understand them. On the other hand, physics informed acoustic analysis methods retain more explanatory power in the relationships between predictions and the data.

The bathymetry of the Monterey Canyon provides a unique observation environment to

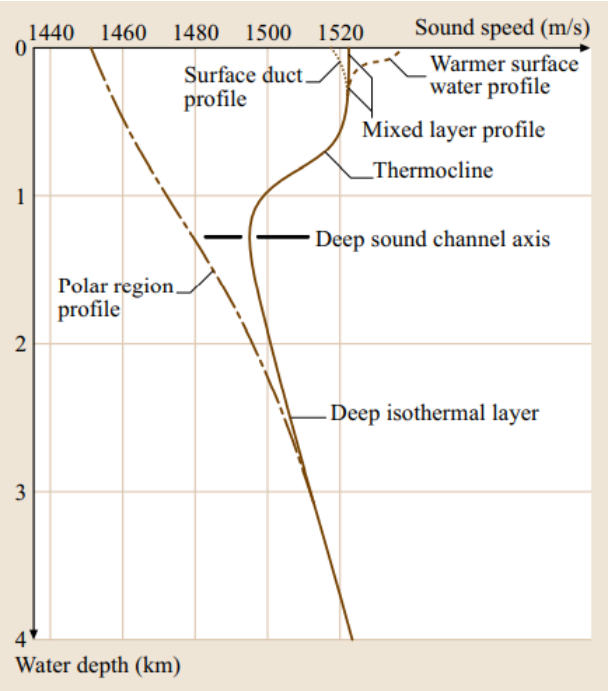

Figure 2.3. Example Sound Speed Profile. (Rossing 2007)

compare the performance of the eigengap estimator in various directions. The sensor rests on a submarine shelf overlooking the depths of the canyon with rising canyon walls to the North, South, and East. The bathymetry drops dramatically to the West following the canyon out to deeper ocean waters. The seafloor contour following the California coast consists of a series of submarine fingers and draws formed by flowing rivers and ancient geological events. These varying bathymetric profiles offer a wide range of experimental cases where acoustic paths may be interrupted or blocked by the diverse seafloor profile, or in other cases completely uninterrupted or channeled directly towards the sensor.

The physics-informed Bellhop ray model (Porter and Bucker 1987) was applied along three different cast directions in order to develop a physical understanding and facilitate some expectation of the ocean environment for comparison to the data driven maximum eigengap estimator. This model used bathymetry data retrieved from GEBCO Compilation Group (2020). The three cast directions are shown in Figure 2.4

The results of the Bellhop model are shown in three different figures 2.5, 2.6, and 2.7. Each

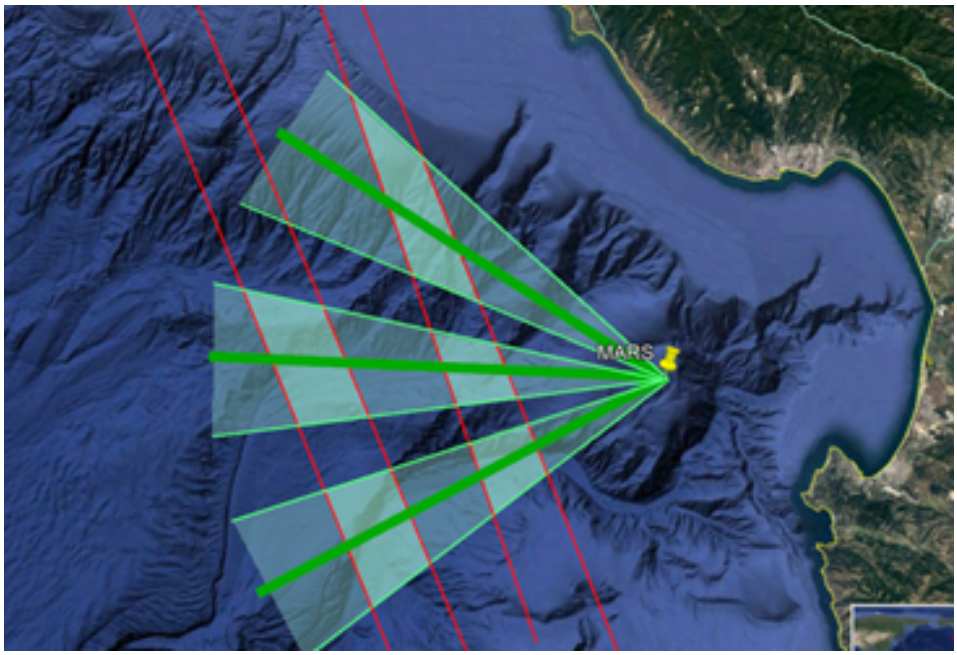

Figure 2.4. Three Casts Directions for the Bellhop Ray Model.

of the three Bellhop casts employs the same sound speed profile; an average sound speed profile for the Monterey Canyon that is shown in the left plot of each figure. A color map of the transmission loss is shown in the top plot of each figure, and the dominant acoustic rays which arrive at the sensor unimpeded are shown in the bottom plot of each figure.

Figure 2.5 shows a relatively steep bathymetric profile, where distant sound sources from the sensor are interrupted by the rising seafloor. Figure 2.6 shows a relatively evenly downward sloping bathymetric profile away from the sensor, and there is less transmission loss due to seafloor interference. The third Figure 2.7 has the most shallow seafloor profile, since this cast runs almost parallel to the California coast line and travels over several submarine fingers and draws. The darker areas in the transmission loss plots indicate where the physics suggests these are quiet zones for the MARS vector sensor. In a military context this is where vessels may not be heard by an observer whose job is to locate enemy ships. In each of the cast directions transmission loss is lowest within ten to 12 kilometers range from the vector sensor. This suggest that surface vessels within that range may be easily detected due to direct path arrivals of the acoustic wave from the source. These observations are compared to the maximum eigengap estimators results in the next chapter.

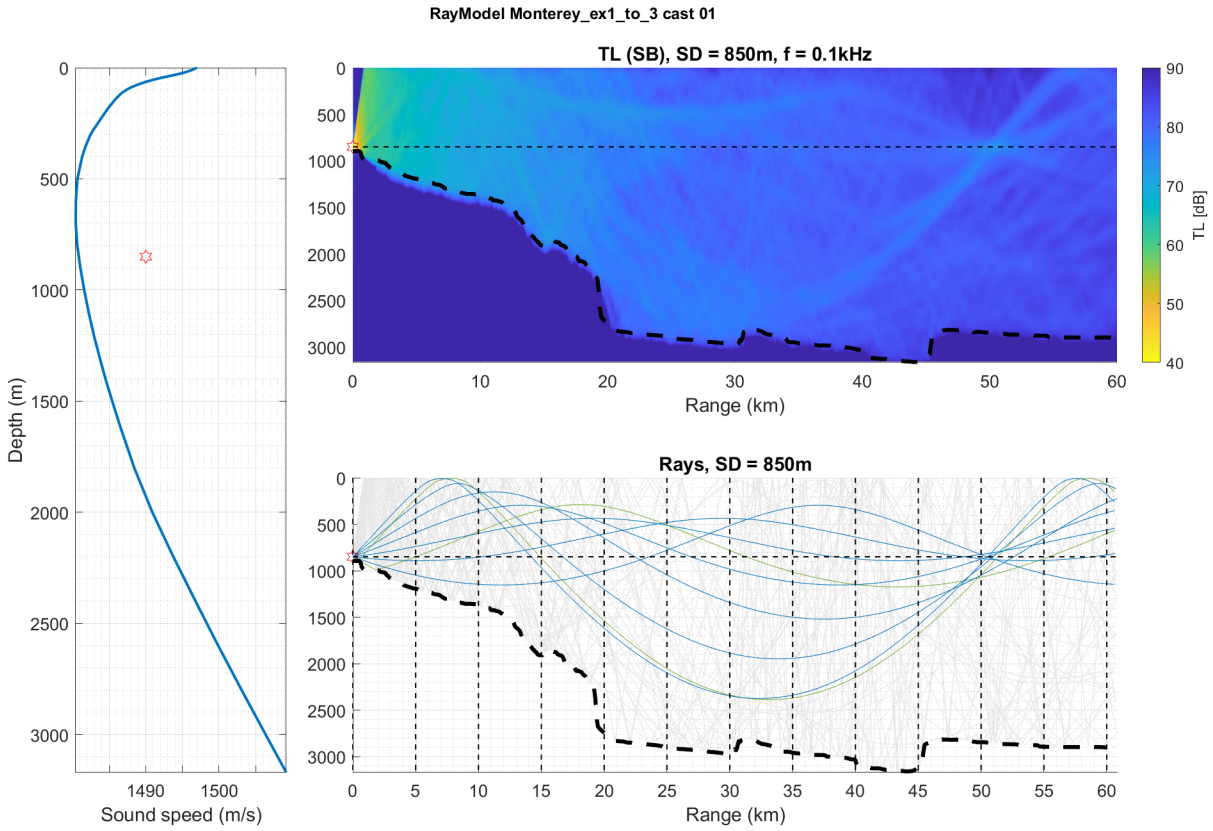

Figure 2.5. Bellhop Ray Model of the Acoustic Transmission Loss along a 235 Degree Cast from the MARS Vector Sensor.

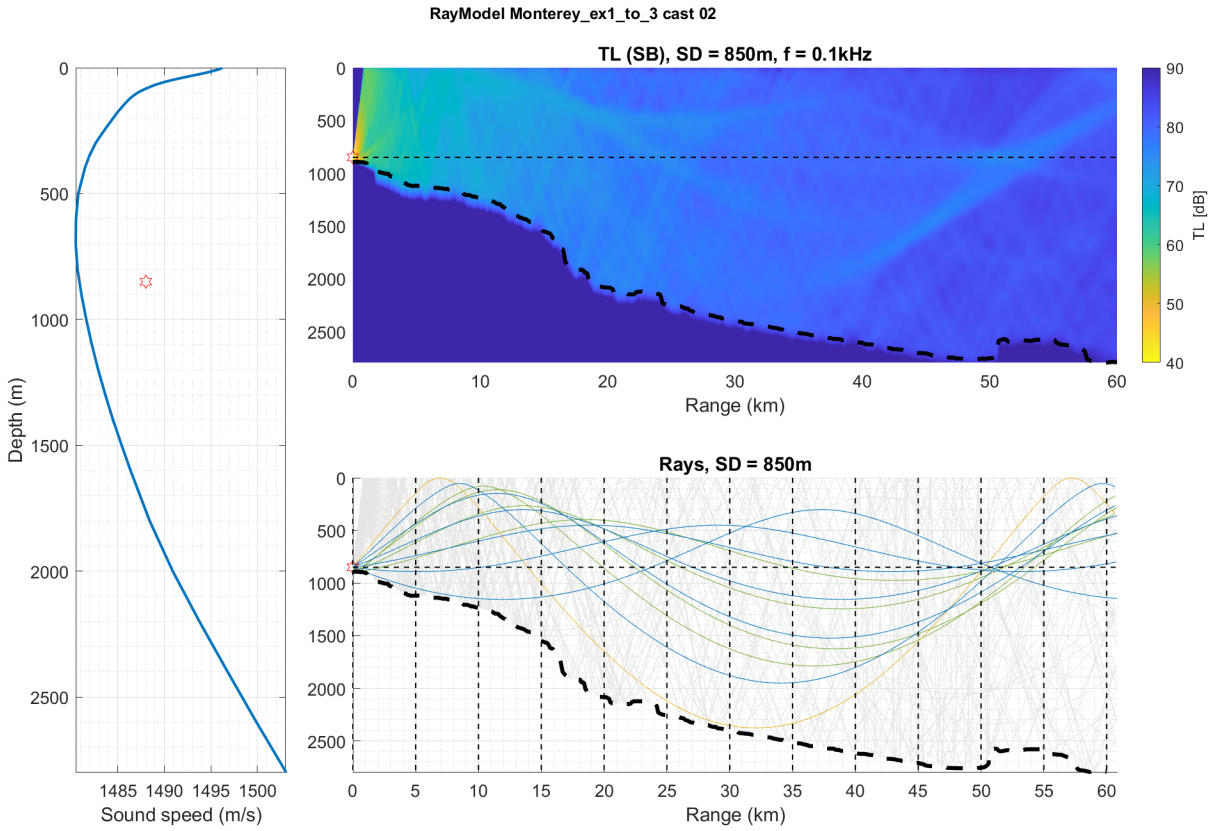

Figure 2.6. Bellhop Ray Model of the Acoustic Transmission Loss along a 270 Degree Cast from the MARS Vector Sensor.

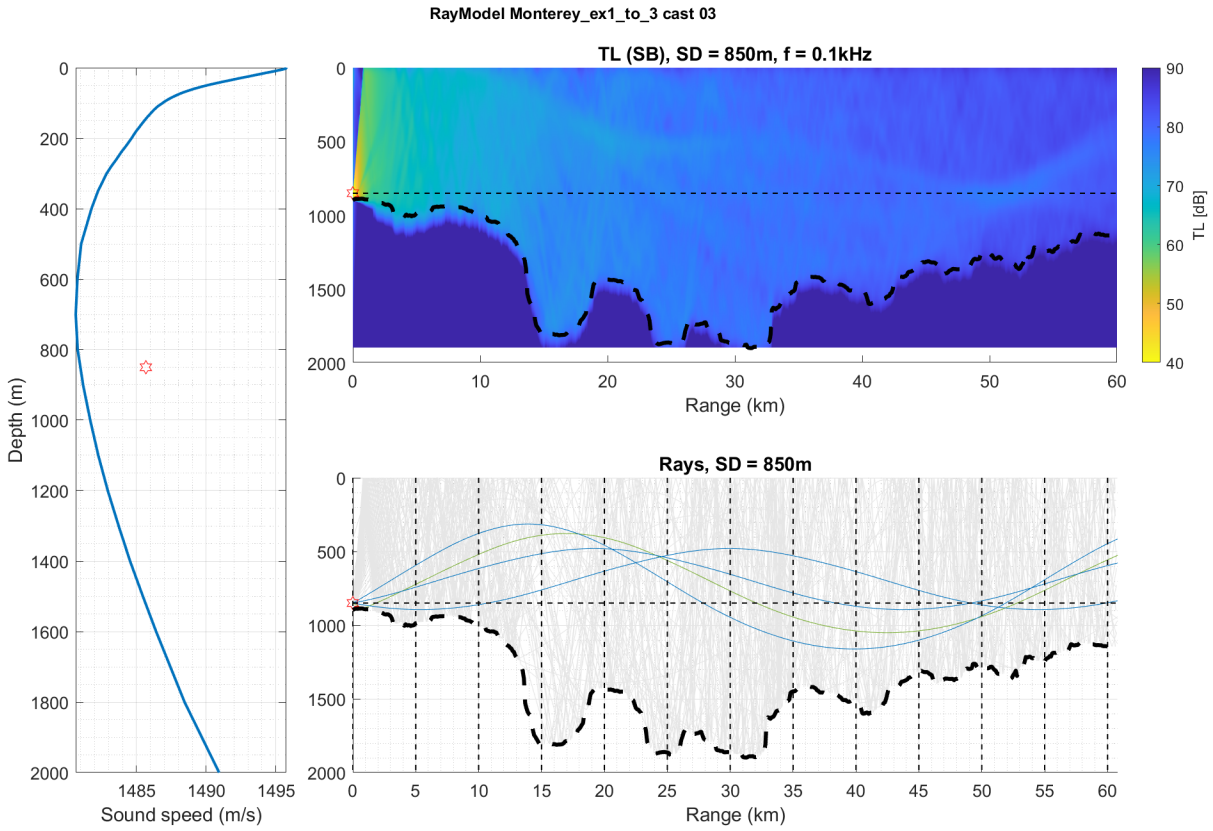

Figure 2.7. Bellhop Ray Model of the Acoustic Transmission Loss along a 300 Degree Cast from the MARS Vector Sensor.

THIS PAGE INTENTIONALLY LEFT BLANK

CHAPTER 3:
The Maximum Eigengap Estimator

The maximum eigengap estimator aggregates the cross-spectral density matrices from a wide band signal and maximizes the signal-to-noise ratio of the resulting signal subspace. This is a novel algorithm for DOA estimation that leverages the x-y channels of the acoustic vector sensor. In this chapter we first present the derivation of the maximum eigengap estimator. Then after a description of the Python code implementation, we present the results of several experiments that test the assumptions and demonstrate the capabilities of the algorithm.

3.1 Derivation

The derivation of the maximum eigengap estimator is somewhat technical, so we present a brief summary here. First, we define the initial frequency domain formulation of the omni-directional pressure received at the sensor as a function of the signal from the source of interest and the ambient noise. Next, we extend the omni-directional formulation to present the cross-power spectral density matrices for the x and y channels of the sensor in equation (3.2). The primary motivation for the maximum eigengap estimator is given by theorem 1, which bounds the difference between the maximum eigenvector of an empirical power matrix and the unit vector in the direction of the SOI. This suggests an optimization problem that will improve the bound in theorem 1 by maximizing the difference between the largest and second largest eigenvalue, the so-called eigengap, over a linear combination of empirical power matrices for a given frequency range. We standardize each power matrix by its trace to account for the fact that lower frequencies contain more noise and have more power, and would exert too much influence in the DOA estimation. Then we define the maximum eigengap estimator in the optimization problem shown in Equation (3.6). In order to find a real expression for the solution of Equation (3.6) we apply the quadratic formula to solve for the roots of the determinant of the characteristic polynomial of the complex eigenvalues of the standardized empirical power matrices. Lastly, we specialize the maximum eigengap estimator to the setting where the weights for the power matrices are constrained to an ℓ_1 norm unit ball, and we show that we can reduce the computational complexity of solving for

the maximum eigengap estimator by reducing it to a problem of finding the determinants of the standardized empirical matrices for each frequency.

The following notation is used for the derivation:

- $\mathbb{S}^1$: The unit circle in $\mathbb{R}^2$.
- $F := \{\omega_1, ..., \omega_N\}$: The set of frequency bins in our short time fourier transform.
- $T := \{t_1, ..., t_n\}$: The set of time bins in our short time fourier transform.
- $X : F \times T \to \mathbb{C}^2$: Our short time fourier transform, as a function of $\omega \in F$ and $t \in T$. Note that this maps to $\mathbb{C}^2$ because the fourier transform has an x and y channel. By convention, we assume that $X(\omega, t)$ is a 2D *column* vector for each $(\omega, t) \in F \times T$.
- $P_X(\omega) := \mathbb{E}\left[\frac{1}{T}\sum_{t\in T} X(t,\omega)X(t,\omega)^H\right]$: A cross-power spectral density at frequency $\omega \in F$, where ^{H} denotes conjugate-transpose. (note that this assumes power time bins are constant of length 1 unit time; for constant time bins of another length we can adjust by a constant factor).
- $\hat{P}_X(\omega) := \frac{1}{T}\sum_{t\in T} X(t,\omega)X(t,\omega)^H$: A periodogram, or empirical cross-power spectral density at frequency $\omega \in F$.
- $\lambda_{min} : \mathbb{C}^{2\times2} \to \mathbb{R}$, $\lambda_{max} : \mathbb{C}^{2\times2} \to \mathbb{R}$, $v_{min} : \mathbb{C}^{2\times2} \to \mathbb{C}^2$, $v_{max} : \mathbb{C}^{2\times2} \to \mathbb{C}^2$ The minimum/maximum eigenvalue (note these are real by the spectral theorem, because each of our matrices is Hermitian (Axler 1997, 7.1 and 7.9)), and their corresponding eigenvectors. As needed, this notation will be extended to Hermitian matrices bigger than 2×2.
- $|||A|||$ denotes to Frobenius norm of a matrix A, i.e. the square-root of the sum of squares of its elements.
- $\bar{z}$ denotes the complex conjugate of a scalar z, or pointwise conjugate of a vector or matrix.

Let $u \in \mathbb{S}^1$ denote the direction from the acoustic vector sensor of some sound source of interest (SOI). Let Y be the short time fourier transform (stft) of the portion of the sensor's omnidirectional channel that can be attributed to the SOI. According to Nehorai and Paldi (1994),

$$X(\omega, t) = u\,Y(\omega, t) + \epsilon(\omega, t) \quad \forall(\omega, t) \in F \times T, \tag{3.1}$$

where ϵ is a noise term that, for our purposes, represents all signal received in the x and y channel that does not originate at our SOI.

Because $u \in \mathbb{S}^1$ is real and $Y(\omega, t)$ is scalar, the cross-power spectral density is

$$P_X(\omega) = E\left[\frac{1}{T}\sum_{t\in T} X(t,\omega)X(t,\omega)^H\right],$$

and plugging in 3.1

$$= E\left[\frac{1}{T}\sum_{t\in T} \|Y(\omega,t)\|^2 u\,u^T - u\,Y(\omega,t)\epsilon(\omega,t)^H - \epsilon(\omega,t)\,(u\,Y(\omega,t))^H + \epsilon(\omega,t)\,\epsilon(\omega,t)^H\right].$$

$$= P_Y(\omega)\,u\,u^T + P_\epsilon(\omega) - \mathbb{E}\left[\frac{1}{T}\sum_{t\in T} Y(\omega,t)\,u\,\epsilon(\omega,t)^H + Y(\omega,t)^*\,\epsilon(\omega,t)\,u^T\right]. \tag{3.2}$$

Collecting the cross-power spectral density matrices of the source and noise components, and **assuming** that $\epsilon(\omega, t)$ and $Y(\omega, t)^*$ are uncorrelated for each t and ω, and that $\epsilon(\omega, t)$ is mean zero for each t, the last term in (3.2) is 0. It follows that

$$P_X(\omega) = P_Y(\omega)\,u\,u^T + P_\epsilon(\omega). \tag{3.3}$$

The following theorem is a direct consequence of (Wainwright 2019, Theorem 8.5) applied to our setting. Informally, it says that when $P_\epsilon(\omega)$ is small the maximum eigenvector of $P_X(\omega)$ is close to the maximum eigenvector of $P_Y(\omega)\,u\,u^T$, which is u.

Theorem 1 *(Wainwright 2019, Theorem 8.5) In* (3.3)*, assume* $P_Y(\omega) > 0$ *and* $|||P_\epsilon(\omega)||| < P_Y(\omega)/2$*. Let* $u^\perp$ *be a unit vector perpendicular to u,* $U = [u, u^\perp]$ *a matrix with columns u and* $u^\perp$*, and* $\tilde{p}$ *the off-diagonal term in* $U^T\,P_\epsilon(\omega)\,U$*. Then denoting by* $v_X(\omega)$ *the maximum eigenvector of* $P_X(\omega)$*, we have*

$$\|v_X(\omega) - u\|_2 \le \frac{2\,|\tilde{p}|}{P_Y(\omega) - 2\,|||P_\epsilon(\omega)|||}. \tag{3.4}$$

Proof. Connecting our notation and that of the reference, we have $\Sigma = P_Y(\omega)\, u\, u^T$, $P = P_\epsilon(\omega)$, $\gamma_1(\Sigma) = P_Y(\omega)$, $\gamma_2(\Sigma) = 0$ (because Σ is rank 1), $\nu = \gamma_1(\Sigma) - \gamma_2(\Sigma) = P_Y(\omega)$, and $\tilde{p}$ is a scalar because Σ is 2×2. The result then follows directly from the statement of (Wainwright 2019, Theorem 8.5). □

Note that, in the bound given in (3.4), we have tighter control on the difference of eigenvectors $v_X(\omega)$ and u when $P_Y(\omega)$ is large and $P_\epsilon(\omega)$ is small. In the empirical sense, the implication for this is that the signal from a SOI would be larger than the ambient ocean noise. This observation motivates our next development.

In the application we consider, vessel detection, the vessel emits a broadband signal. This means that we expect $P_Y(\omega)$ to be large for a *range* of ω. Thus we extend (3.3) by searching for a weighted combination of the power matrices that gives a tighter bound in (3.4). This is narrow band aggregation of the frequencies attributing to the broadband signal where the maximum eigenvector points towards the SOI. Namely, we propose solving, for some norm $\|\cdot\|$, the following problem.

$$\max_{a \in \mathbb{R}^{|F|}} \lambda_{max}\left(\sum_{\omega \in F} a_\omega P_Y(\omega) u u^T\right)$$

$$\text{s.t.} \quad \|a\| \leq 1, \quad a \geq 0$$

If we were to find an optimal linear combination of coefficients a, we improve the bound in (3.4) by replacing $P_Y(\omega)$ with $\sum_{\omega \in F} a_\omega P_Y(\omega)$. Because $\lambda_{min}\left(P_Y(\omega)\, u\, u^T\right) = 0$, this problem is equivalent to

$$\max_{a \in \mathbb{R}^{|F|}} \lambda_{max}\left(\sum_{\omega \in F} a_\omega P_Y(\omega)\, u\, u^T\right) - \lambda_{min}\left(\sum_{\omega \in F} a_\omega P_Y(\omega)\, u\, u^T\right)$$

$$\text{s.t.} \quad \|a\| \leq 1, \quad a \geq 0.$$

Since $P_Y\, u\, u^T$ is unknown, the approximation $P_X(\omega)$ can be implemented into

$$\max_{a \in \mathbb{R}^{|F|}} \lambda_{max}\left(\sum_{\omega \in F} a_\omega P_X(\omega)\right) - \lambda_{min}\left(\sum_{\omega \in F} a_\omega P_X(\omega)\right)$$

$$\text{s.t.} \quad \|a\| \leq 1, \quad a \geq 0.$$

One issue with this formulation is that some frequencies (the lower ones) have much more power than others, so they dominate this calculation in spite of the fact that more noise also occurs in those frequencies. To remedy this, we standardize each power matrix $P_X(\omega)$ to have trace 1. We denote these standardized power matrices by $Q(\omega)$,

$$Q_X(\omega) = \frac{P_X(\omega)}{\text{trace}\,(P_X(\omega))}. \tag{3.5}$$

Alternatively, we could standardize each power matrix to have minimum eigenvalue 1. In that case, the maximum eigenvalue approximates the SNR of the power matrix.

Lastly, we actually don't know $P_X(\omega)$, since it is a population cross power spectral density, so we replace it by its periodogram. We extend the notation in (3.5) as one would expect, so that $\hat{Q}_X(\omega) = \hat{P}_X(\omega)/\text{trace}\left(\hat{P}_X(\omega)\right)$.

$$\max_{a\in\mathbb{R}^{|F|}} \lambda_{max}\left(\sum_{\omega\in F} a_\omega \hat{Q}_X(\omega)\right) - \lambda_{min}\left(\sum_{\omega\in F} a_\omega \hat{Q}_X(\omega)\right) \tag{3.6}$$

$$\text{s.t.} \quad \|a\| \leq 1, \quad a \geq 0.$$

We define the *maximum eigengap estimator* as the maximum eigenvector $v_{max}\left(\sum_{\omega\in F} \hat{a}_\omega \hat{Q}_X(\omega)\right)$, where $\hat{a}$ denotes the maximizer in (3.6).

There are various ways to solve (3.6) for different choices of norms. However, this thesis only explores the ℓ_1 norm in the estimator. Next, we derive the following important proposition.

Proposition 1 *The objective in* (3.6) *is the square root of a convex quadratic function of* a.

Proof. The key to this result is noting that the matrices are 2×2. Denote the entries of $\hat{Q}_X(\omega)$ by

$$\hat{Q}_X(\omega) = \begin{pmatrix} q_\omega & r_\omega \\ \bar{r}_\omega & s_\omega \end{pmatrix},$$

where we have used the conjugate symmetry of $\hat{Q}_X(\omega)$ in the off-diagonal terms. The

complex eigenvalues

$$\lambda_{max}\left(\sum_{\omega\in F} a_\omega \hat{Q}_X(\omega)\right) \quad \text{and} \quad \lambda_{min}\left(\sum_{\omega\in F} a_\omega \hat{Q}_X(\omega)\right)$$

are given by the zeros of the characteristic polynomial for $\sum_{\omega\in F} a_\omega \hat{Q}_X(\omega)$,

$$\det\begin{pmatrix} \sum_{\omega\in F} a_\omega q_\omega - \lambda & \sum_{\omega\in F} a_\omega r_\omega \\ \sum_{\omega\in F} a_\omega \bar{r}_\omega & \sum_{\omega\in F} a_\omega s_\omega - \lambda \end{pmatrix} = 0. \tag{3.7}$$

These roots can be computed explicitly using the quadratic formula. Expanding the determinant in (3.7),

$$\left(\sum_{\omega\in F} a_\omega q_\omega - \lambda\right)\left(\sum_{\omega\in F} a_\omega s_\omega - \lambda\right) - \left|\sum_{\omega\in F} a_\omega r_\omega\right|^2$$

$$= \lambda^2 - \left(\sum_{\omega\in F} a_\omega q_\omega + \sum_{\omega\in F} a_\omega s_\omega\right)\lambda + \left(\sum_{\omega\in F} a_\omega q_\omega\right)\left(\sum_{\omega\in F} a_\omega s_\omega\right) - \left|\sum_{\omega\in F} a_\omega r_\omega\right|^2 \tag{3.8}$$

We know that the roots of this expression are *real*, because they are the eigenvalues of the conjugate symmetric matrix $\sum_{a\in F} a_\omega \hat{Q}_X(\omega)$. The quadratic formula then gives that the difference between the maximum and minimum eigenvalues is the discriminant of the quadratic in (3.8), which is nonnegative because the eigenvalues are real.

$$\sqrt{\left(\sum_{\omega\in F} a_\omega \left(q_\omega + s_\omega\right)\right)^2 - 4\left(\left(\sum_{\omega\in F} a_\omega q_\omega\right)\left(\sum_{\omega\in F} a_\omega s_\omega\right) - \left|\sum_{\omega\in F} a_\omega r_\omega\right|^2\right)}. \tag{3.9}$$

Because we maximize this expression in (3.6), and it is always nonnegative, we can instead maximize the square of (3.9)

$$\left(\sum_{\omega\in F} a_\omega \left(q_\omega + s_\omega\right)\right)^2 - 4\left(\left(\sum_{\omega\in F} a_\omega q_\omega\right)\left(\sum_{\omega\in F} a_\omega s_\omega\right) - \left|\sum_{\omega\in F} a_\omega r_\omega\right|^2\right). \tag{3.10}$$

Because each $\hat{Q}_X(\omega)$ has unit trace, $q_\omega + s_\omega = 1$. Therefore (3.10) can be rewritten

$$\left(\sum_{\omega\in F} a_\omega\right)^2 - 4\left(\left(\sum_{\omega\in F} a_\omega q_\omega\right)\left(\sum_{\omega\in F} a_\omega s_\omega\right) - \left|\sum_{\omega\in F} a_\omega r_\omega\right|^2\right). \tag{3.11}$$

Expanding (3.11), we have

$$\sum_{\omega_1\in F}\sum_{\omega_2\in F} a_{\omega_1}a_{\omega_2} - 4\left(a_{\omega_1}q_{\omega_1}s_{\omega_2}a_{\omega_2} - a_{\omega_1}r_{\omega_1}\bar{r}_{\omega_2}a_{\omega_2}\right) \tag{3.12}$$

Define a matrix $\tilde{R} \in \mathbb{C}^{|F|\times|F|}$ with

$$\tilde{R}_{\omega_1,\omega_2} = 1 - 4\left(q_{\omega_1}s_{\omega_2} + r_{\omega_1}\bar{r}_{\omega_2}\right),$$

so that the quadratic form $a^T\,\tilde{R}\,a$ gives (3.12).

Next we apply two common tricks to produce a real symmetric quadratic form R which is equal to the quadratic form given by $\tilde{R}$. First, note that expression (3.10) is real, because a_ω is real, and q_ω and s_ω are also real (recall that $\hat{Q}_X(\omega)$ is conjugate symmetric). Hence (3.10) is equal to its own conjugate. Because (3.12) and (3.10) are equal, it follows that

$$\overline{a^T\tilde{R}a} = a^T\tilde{R}a.$$

Therefore $\frac{1}{2}a^T\left(\tilde{R} + \overline{\tilde{R}}\right)a = a^T\tilde{R}a$, where we note that $\frac{1}{2}\left(\tilde{R} + \overline{\tilde{R}}\right)$ is *real*. In a similar fashion, because $\frac{1}{2}a^T\left(\tilde{R} + \overline{\tilde{R}}\right)a$ is a scalar, it is equal to its own transpose. It follows that

$$\frac{1}{2}a^T\left(\tilde{R} + \overline{\tilde{R}}\right)a = \frac{1}{2}a^T\left(\tilde{R} + \overline{\tilde{R}}\right)^T a.$$

Therefore

$$\frac{1}{4}a^T\left(\left(\tilde{R} + \overline{\tilde{R}}\right) + \left(\tilde{R} + \overline{\tilde{R}}\right)^T\right)a = a^T\tilde{R}a.$$

Setting $R = \frac{1}{4}\left(\left(\tilde{R} + \overline{\tilde{R}}\right) + \left(\tilde{R} + \overline{\tilde{R}}\right)^T\right)$, we have a real symmetric quadratic form which is equal to the quadratic form given by $\tilde{R}$.

Finally, we note that R is convex because $a^T Ra$ is nonnegative for any choice of a. This follows from the derivation of (3.9), in which we note that the discriminant is nonnegative because the eigenvalues of the conjugate symmetric matrix $\sum_{a\in F} a_\omega \hat{Q}_X(\omega)$ must be real. □

Proposition 1 allows us to write (3.6) in an alternate form, where instead of maximizing the objective in (3.6) we maximize its square,

$$\max_{a\in\mathbb{R}^{|F|}} a^T Ra \tag{3.13}$$
$$\text{s.t.} \quad \|a\| \leq 1 \quad a \geq 0.$$

This is the form of the problem which we analyze in the remainder.

3.1.1 Applying the ℓ_1 Constraint

Before proceeding we mention an important result which will be useful in the remainder. Recall that an *extreme* point of a convex set is a zero dimensional face; a vertex when the convex set is polyhedral.

Theorem 2 *(Rockafellar 2015, Corollary 32.3.4) Let f be a convex function, and let C be a nonempty polyhedral convex set contained in* $\text{dom} f$*. Suppose that C contains no lines, and that f is bounded above on C. Then the supremum of f relative to C is attained at one of the (finitely many) extreme points of C.*

When the norm in (3.13) is the ℓ_1 norm, then the positivity constraint allow us to write (3.13) as

$$\max_{a\in\mathbb{R}^{|F|}} a^T Ra \tag{3.14}$$
$$\text{s.t.} \quad \sum_{\omega\in F} a_\omega \leq 1, \quad a \geq 0.$$

The extreme points of this feasible region are shown to be points a such that $a_\omega = 1$ for some ω and 0 elsewhere (and the 0 vector) in the proposition below. Recall[1] that for a convex set C, $x \in C$ is an *extreme point* of C if and only if the only way to express x as a convex combination $(1-\lambda)y + \lambda z$ for $y, z \in C$ and $0 < \lambda < 1$ is to take $y = z = x$.

[1] See e.g. (Rockafellar 2015, Section 18)

Proposition 2 *The extreme points of the constraint set in* (3.13) *is the set* $\{0\} \cup \{e_j\}_{j=1}^{|F|}$, *where each* $e_j = 1$ *at index* j *and* 0 *otherwise.*

Proof. First, we show that the listed set of points is extreme. Note that the non-negativity and ℓ_1 constraints in the constraint set imply that each of the elements are bounded by 1 coordinate-wise. In the case of the standard basis vectors, this gives that for a convex combination of some y and z to be 1 at the jth index, neither y not z can be less than 1 at the jth. From this reasoning we conclude that the jth coordinate of y and z must be 1, so that $y = z = e_j$. The zero vector is obviously an extreme point, because the non-negativity constraint makes it impossible for a convex combination of nonzero vectors to be zero. □

Proposition 2, combined with Theorem 2 and Proposition 1 give that the minimizing a in (3.13) is one of $\{0\} \cup \{e_{\omega_j}\}_{\omega_j \in |F|}$. Note that

$$e_{\omega_j}^T R e_{\omega_j} = R_{\omega_j,\omega_j} = 1 - 4(q_{\omega_j} s_{\omega_j} + |r_{\omega_j}|^2)$$

$$= 1 - 4 \det \hat{Q}_X(\omega_j)$$

It follows that the maximizer of the objective function is e_{ω_j}, where $j \in \operatorname{argmin}_{\omega_j \in |F|} \left(\det \hat{Q}_X(\omega_j) \right)$, i.e. the standard basis vector corresponding to the empirical power matrix with the smallest determinant. This is a significant result, because we have reduced (3.13), a problem of maximizing a convex objective over a convex constraint (which is NP-hard in general (Zwart 1974)), to one of finding the minimum determinants from a set of $|F|$ 2×2 matrices.

3.2 Python Implementation

This section outlines the tools, and programmatic workflow that was used in computing bearing estimates. The programming language Python was used to run the maximum eigengap estimator. Additionally, most of the experiments were run on the Hamming HPC to exploit the computational power and experiment with the algorithm's scalability.

Several modules were written to query the data and accomplish the analysis. Other well known open source packages were used to perform computational tasks. The module "find_and_slice" developed by Kim (2020) and written in Python/Cython, retrieves the

acoustic data after it is given a timestamp, an acoustic record length, and the option to provide calibrated or uncalibrated data. Since the AIS data is stored in an SQLite database, the Python wrapper SQLite3 was used to execute database queries for timestamps. We scripted the "AIStools" module to implement a variety of useful SQLite queries of the AIS data. The "max_eigen" module executes the maximum eigengap estimator algorithm to solve the optimization problem. The "max_eigen" module also provides options for ℓ_1 and ℓ_2 norm constraints in (3.13). The open source Python packages "scipy", "numpy", and "pandas" were used in conjunction with those previously mentioned.

The programmatic workflow execution of the maximum eigengap estimator is as follows:

1. Query the AIS data for relevant timestamps using the AIStools module.
2. Import the query into a pandas dataframe to filter and/sort the data as required.
3. Pass the timestamps to the "find_and_slice" module to query the acoustic record from the vector sensor.
4. Utilizing the "scipy" package, compute the short-time-fourier transform of the signal and return the fourier transforms from the x and y channels.
5. Compute the empirical power matrices (as periodograms (Rossing 2007)) from the fourier transforms of the x and y channels.
6. Pass the power matrices, and the desired frequency bounds for the power matrices, to the "max_eigen" module to compute an estimate of the vector pointing toward the SOI.
7. Convert the complex vector estimate to a real value in degrees to produce an estimate of the bearing.

3.3 Experimental Results

This section presents the results of the experiments that were conducted to test the performance of the maximum eigengap estimator. First, we apply the estimator to acoustic records that contain only a single vessel within 10 km range of the sensor. Next, the performance of the sensor is tested when there are two vessels in the acoustic record during the same timestamp, and both vessels are within 10 km of the sensor but at different ranges. Third, we compare the performance of the maximum eigengap estimator to the predictions produced by the Bellhop ray model, using the same cast directions and distances from the source

to the sensor (see Figure 2.4). Next, the frequency sensitivity of the maximum eigengap estimator is explored. Lastly, we produce a map of the maximum eigengap estimator over the data set to demonstrate the scalability of the algorithm.

Each of the below experiments were performed on the uncalibrated and calibrated vector sensor data. Eastward AIS observations were omitted due to the fact that there will likely be acoustic reflections from the Monterey Canyon, adding error in the estimator, and for the fact that the majority of large vessels in the vicinity of the sensor appear westward towards the North to South running shipping lanes. In addition, the estimator itself is only designed to estimate a signal subspace, which leaves 180 degree ambiguity due to the fact that eigenvectors are only unique up to change in sign. This is a common restriction on signal subspace methods, and is not unique to the maximum eigengap estimator (Nehorai and Paldi 1994).

3.3.1 Single Ship Experiments

The first experimental tests for the maximum eigengap estimator were performed using 234 timestamps that contained a single vessel in the AIS record. Each of the vessels in the AIS record are within a range of 10 km, and with longitude coordinates West of the sensor. The frequency bounds for the estimator were set between 100 and 300 Hz, and the acoustic samples are five minutes long. Figure 3.1 shows the performance of the estimator on the uncalibrated data (a) and calibrated data (b) as previously discussed in Section 2.1. The forty-five degree dashed red line shows where perfect estimations should lie. Each estimation is colored by the vessels with MMSI's occurring more the 20 times in the AIS record.

The estimator appears to perform better on the uncalibrated data. What follows are the summary observations of Figure 3.1 (a). The majority of the estimates lie near the true bearing. We see Vessel 2 is consistently over estimated between 50 and 75 degrees. There is a clustering of Vessel 1 with an estimate near -90 degrees from the sensor. It is likely Vessel 1 is either traveling at this bearing, or is stationary during these observations timestamps. We also see that bearings greater than -100 degrees are both over and underestimated, while the majority of bearings less than -100 degrees are mostly overestimated.

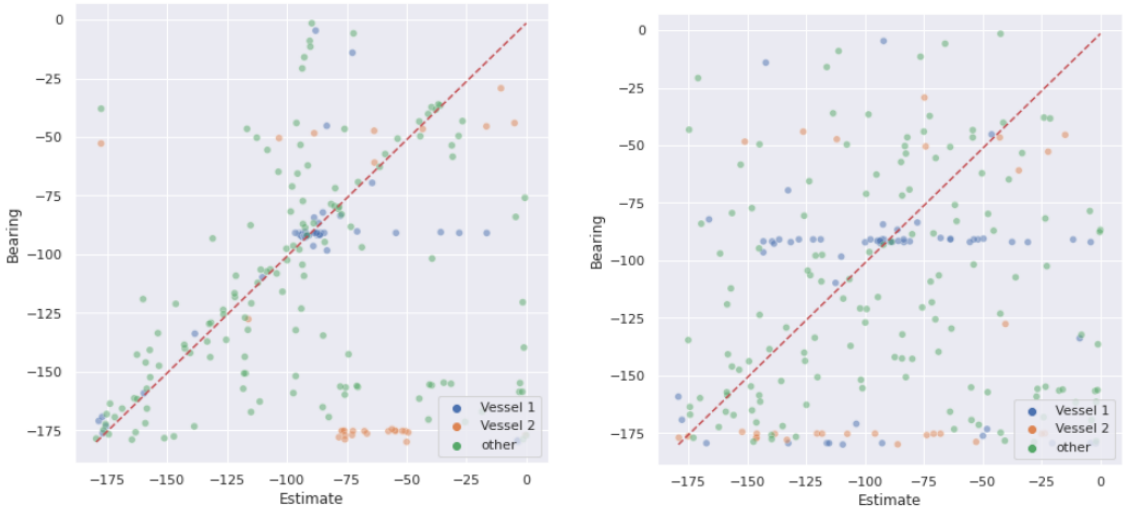

(a) Uncalibrated Vector Sensor Data

(b) Calibrated Vector Sensor Data

Figure 3.1. Maximum Eigengap Estimator Performance: Single-Unique Observations of Vessels within 10 km

The histograms of errors for the maximum eigengap estimator on these 234 observations are shown in Figure 3.2. The error was calculated as the $Estimate - Truth$. The comparison between the histograms in Figure 3.2 show the estimator generally produces lower error on the uncalibrated data.

It is not readily obvious why the maximum eigengap estimator produces higher error on the calibrated data. However, one possible reason for this discrepancy is that the linear operation of the calibration curves amplifies electrical noise present in the sensor. This noise is broadband with a peak frequency at 500 Hz. Since the electrical noise is broadband and constant, it adds non-mean zero noise in the cross-power spectral density matrix (equation 3.3) at the frequency ranges the maximum eigengap estimator is discriminating causing error in the bearing estimations. Alternatively, there may be a discrepancy not captured in the deployment of the algorithm that causes the maximum eigengap estimator to perform less accurately on the calibrated data.

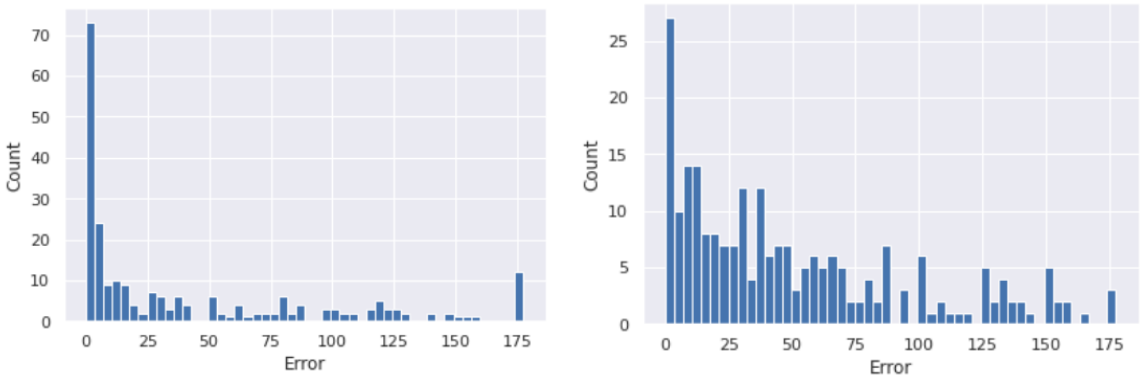

(a) Uncalibrated Vector Sensor Data (b) Calibrated Vector Sensor Data

Figure 3.2. Maximum Eigengap Estimator Performance Histogram: Single-Unique Observations of Vessels within 10 km

3.3.2 Multi-Ship Experiments

The following experiment tests the ability of the maximum eigengap estimator in Equation (3.6) to point towards the loudest noise source in the x and y channels from the vector sensor. Recall Equation (3.3), and theorem 1. If there are multiple noise sources in the acoustic record, and those sources are within direct path arrival-range of the sensor, then we should expect the estimator to provide bearing estimates for the loudest, and/or possibly the closest, vessel. To test this hypothesis, we collected timestamps where the acoustic record should contain two different vessels. This was done by filtering the AIS timestamps for vessels within 10 km, and then keeping only timestamps that showed a vessel between 0-3 km (which we identify as the "near ship") and a vessel between 3-10 km (we identify as the "far ship"). This resulted in 512 timestamps associated with their five-minute acoustic records. The maximum eigengap estimator was computed over these observations, and the estimates were compared with the AIS provided bearings for both the *near* and *far* vessel. These results are shown in Figure 3.3 for the uncalibrated (a) and calibrated (b) data. The frequency lower and upper bounds for the maximum eigengap estimator was 100 and 300 Hz respectively.

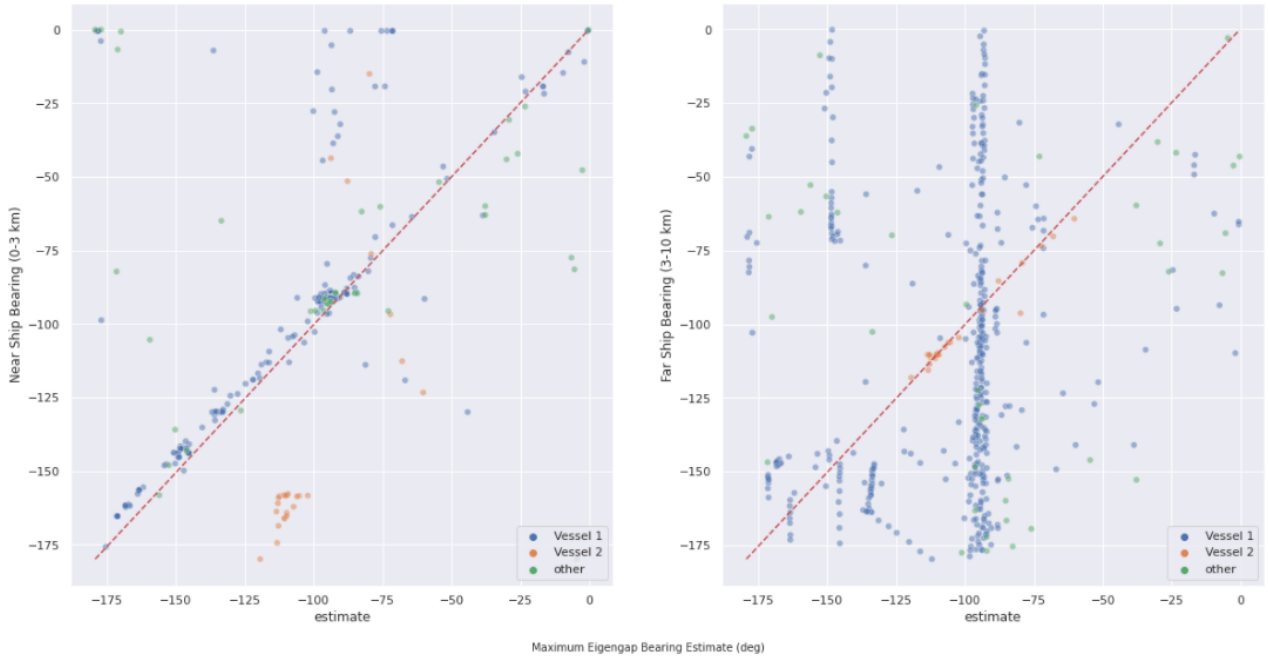

(a) Uncalibrated Vector Sensor Data

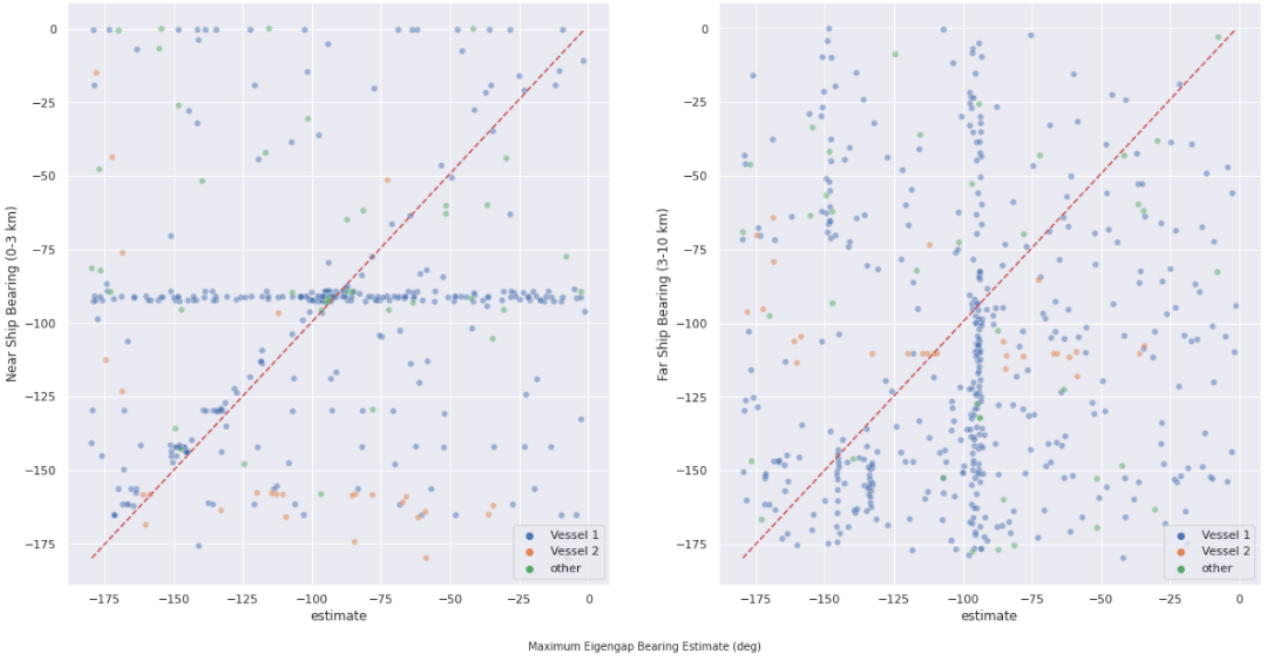

(b) Calibrated Vector Sensor Data

Figure 3.3. Maximum Eigengap Estimator Performance: Dual Observations of Vessels within 10 km. The red line indicates 'perfect' estimation.

Figure 3.3 shows the maximum eigengap estimator produces accurate estimates for the bearings of SOI signals produced by ships within the 0-3 km range. The uncalibrated data produces more accurate and interpretable results. The observations were labeled according to their MMSI by color. We see in the "Near" ship uncalibrated results that a cluster of observations attributed to Vessel 2 are poorly estimated near an estimated bearing between -100 and -125 degrees, with the truth between -150 and -177 degrees. However, when compared to the same uncalibrated "Far" ship results it appears the estimator accurately identifies the bearing of Vessel 2. Possible reasons for this are: the vessel is close to the 3 km limit, Vessel 2 may be louder than the closer vessel with the same timestamp, or possibly the closer vessel's acoustic path is interrupted and does not reach the sensor. When the maximum eigengap estimator fails, it prefers to produce estimates near the -90 degree bearing as shown by the vertical cluster of estimates in the "Far" ship plots. This source of error is unknown and provides potential for future work.

3.3.3 Bellhop Ray Model Comparison

The Bellhop Model discussed in Chapter 2 provided a starting point for understanding the acoustic environment near the MARS vector sensor. The Bellhop Model experiment design was replicated for the maximum eigengap estimator, using three cast directions as cases for analysis. The AIS timestamps were filtered to collect approximately 2000 single vessel observations within the 20 degree fans along each of the three cast directions (-120 degree, -90 degrees, and -60 degrees) as shown in Figure 2.4. The maximum distance for each of the observations is 80 kilometers to ensure each of the 20 degree fans includes the shipping lanes that run parallel to the California coast. After the bearing estimates were computed by the maximum eigengap estimator, the estimates were grouped by 3 km bins in order to compute the Mean Absolute Angular Deviation (MAAD). We define MAAD as: $\frac{1}{n}\sum_{i=1}^{n}|Bearing\ Estimate_i - Bearing\ Truth_i|$, where n is the number of estimates in the 3 km bin. The frequency lower and upper bound for the maximum eigengap estimator were 100 Hz and 300 Hz, respectively. The MAAD for the 3 km bins along each of the cast directions are shown along with the associated bin histograms in Figure 3.4 for both the uncalibrated (a) and calibrated vector sensor data (b).

Since the uncalibrated data shows more interpretable results those are discussed here first. In each of the plots the vertical red lines indicate the shipping channels also identified by the

red lines in 2.4. The -90 deg bearing cast shows slightly better estimation all around. This profile has less bottom interference and may allow more direct acoustic path arrivals from the source to the sensor. Each of the cast directions show relatively lower MAAD up to about 10 km. This coincides with the direct path arrival limit as estimated by the Bellhop model. We also see a reduction in MAAD at candidate locations for indirect path arrivals from surface sources: between 20-30 km, and 40-50 km (bearing -120 deg); bearing -90 does not show significant improvement at any range (possibly between 35-3 7km), and between 30-40 km (bearing -60 deg). These improvements coincide with the shipping lanes, thus significantly increasing the number of observations in the denominator of the MAAD.

Consistent with the previous experiment, the maximum eigengap estimator does not perform as well on the calibrated data. Interestingly, the number of observations (identified by vessels near the shipping lanes) does not seem to reduce the MAAD nor show an increased overall performance in the maximum eigengap estimator.

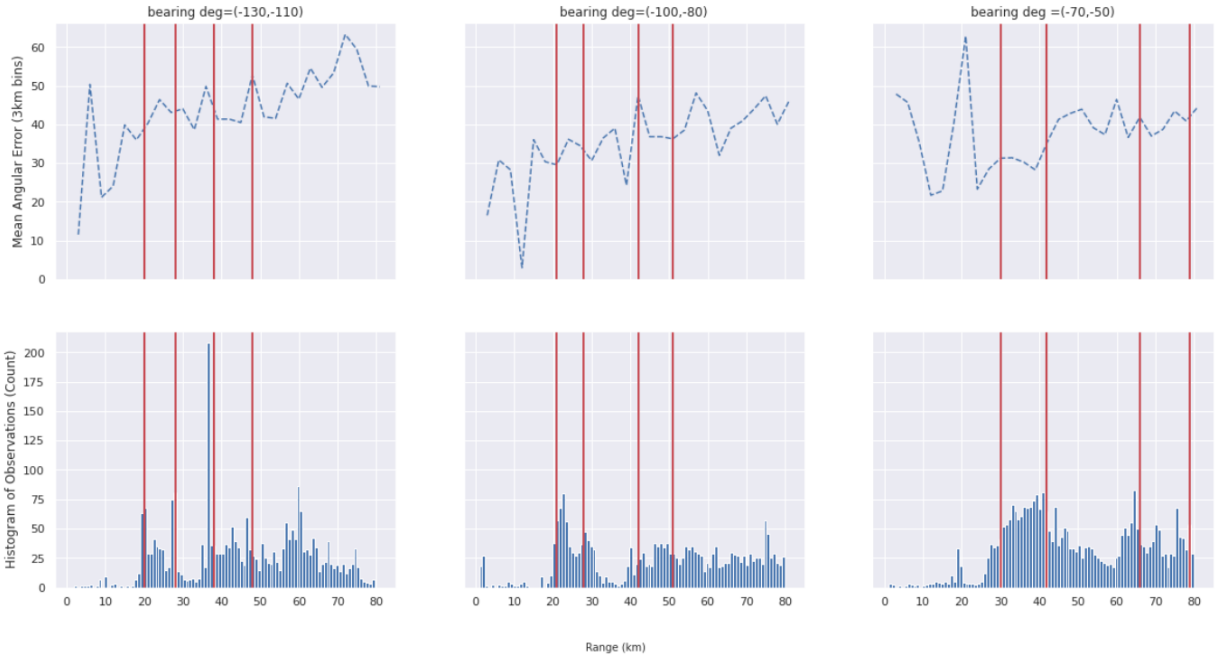

(a) Uncalibrated Vector Sensor Data

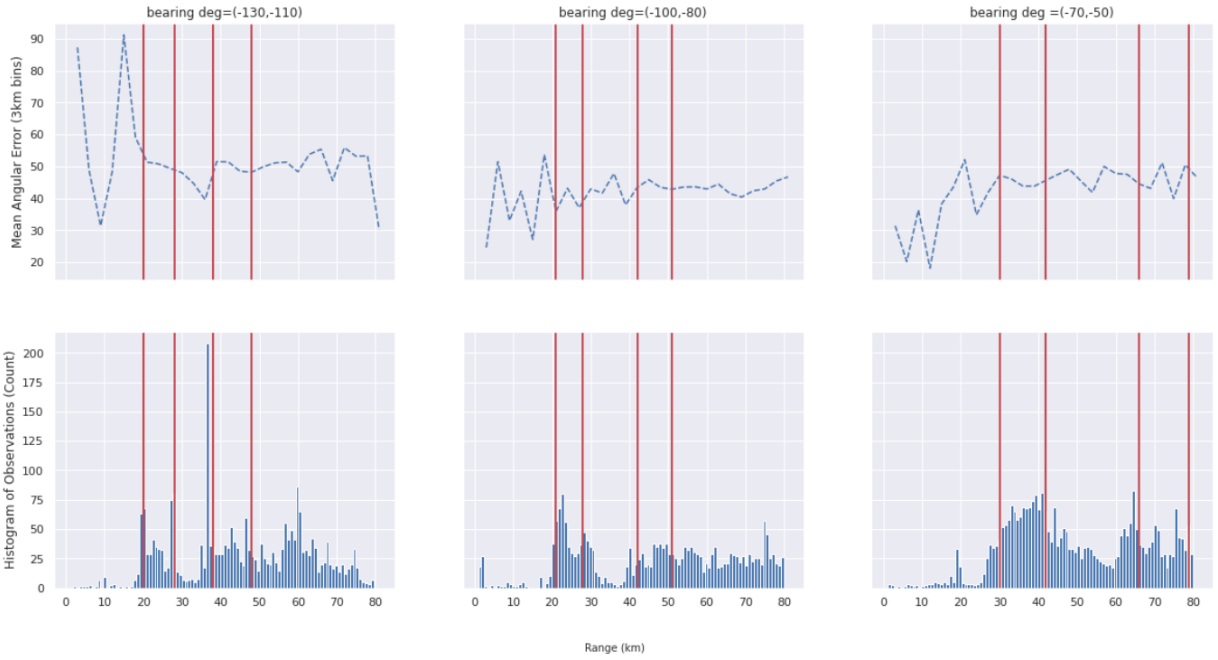

(b) Calibrated Vector Sensor Data

Figure 3.4. Maximum Eigengap Estimator: Performance along three different cast directions (-120, -90, -60 degree fans) on uncalibrated and calibrated acoustic data. Red lines indicate shipping transit lanes

3.3.4 Frequency Sensitivity

In equation (3.5) we introduce the standardization of the cross-spectral power matrices to overcome frequency dependent contributions of noise. Also, as shown in Figure 1.1, empirical acoustic measurements of the ocean contain a wide range noise contributing frequencies. It is therefore prudent, if not scientifically required, to analyze the maximum eigengap estimator's performance by varying the upper and lower limit of the frequency selection range. Thus, we explored the following experiment. For the timestamps of the acoustic record, we continued the pattern of extracting AIS timestamps along the three cast direction previously mentioned in section 3.3.3. However, each of the 20 degree sets of observations were iterated over using a range of lower and upper frequency bounds, starting at 50 Hz and ending at 650 Hz, with $\Delta\omega$ = 25 Hz. The estimates were binned by 3 km intervals and the MAAD was computed for each 3 km range x 25 Hz frequency bin. These results for the uncalibrated (a) and calibrated acoustic data (b) are shown in Figure 3.5.

We used the MAAD shown by the colorbar in Figure 3.5 to explore the accuracy of the maximum eigengap estimator across three cast directions. Again, the results of the maximum eigengap estimator on the uncalibrated data show better performance and are more interpretable. However, both sets of experiments show better performance where the source is at closer distances to the sensor (less than 12 km) across all frequencies and in each of the three directions. This is likely due to direct path acoustic arrivals from sources near the sensor. Along the -90 degree casts path we see better performance at low frequency ranges across all distances. In the results on the uncalibrated data, there appears to be a transmission-loss effect at 12-15 km across all frequencies and then an improvement immediately after that at 15-18 km. At closer distances we also see an increase in MAAD at higher frequencies.

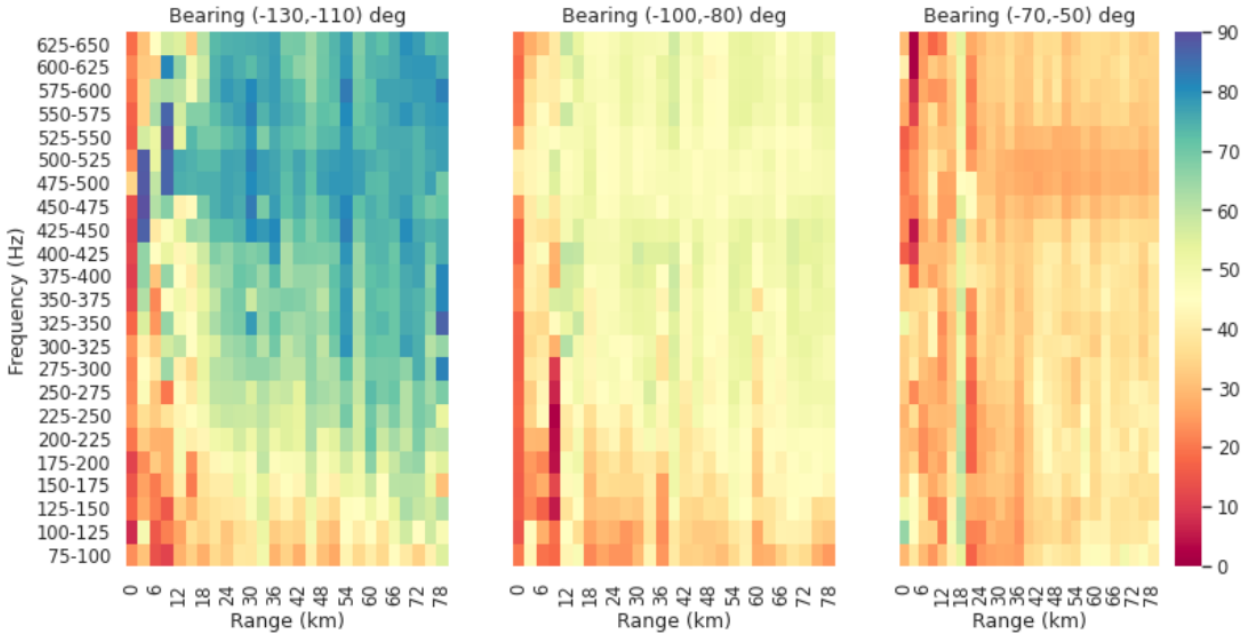

(a) Uncalibrated Vector Sensor Data

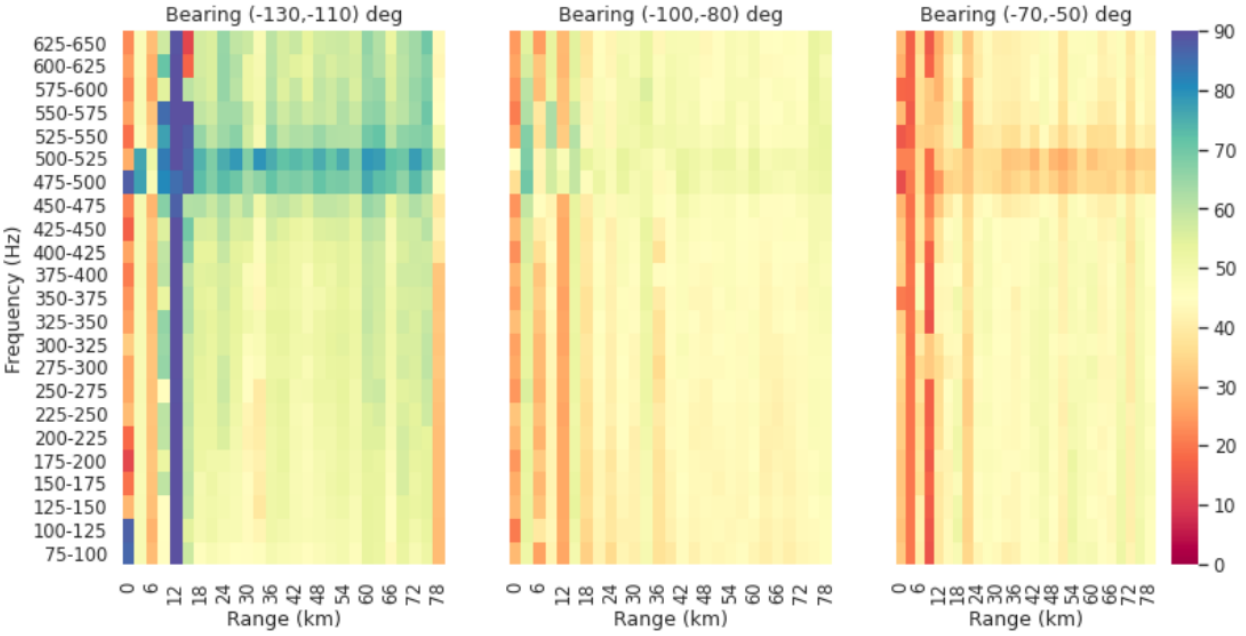

(b) Calibrated Vector Sensor Data

Figure 3.5. Maximum Eigengap Estimator Frequency Sensitivity: Performance along three different cast directions (-120, -90, -60 degree fans) on uncalibrated and calibrated acoustic data. Colorbar is MAAD in 3 km by 25 Hz bins.

3.3.5 Maximum Eigengap Estimator at Scale

One of the advantages of pursuing a data-driven approach to acoustic localization is the relative ease in which we can scale the estimates. The following experiment, shown in Figure 3.6, demonstrates the scalability of the estimator by using the historical acoustic record to generate a map of the maximum eigengap estimator's performance in MAAD. This map shows areas of detection by low MAAD, where a passing vessel's bearing from the sensor can be accurately estimated by the maximum eigengap estimator. The contrast to physics-informed analysis is that physical models can produce similar maps, but as mentioned before, they require detailed assumptions about the ocean environment and source frequency. Also, more complex physical models require significantly more computation time. The map produced here is purely based on the data received at the sensor. This type of map has the unique utility which suggests that, given a sufficiently large data set of true bearings, we can create an operational picture of the geographic areas that vessels transit through and our ability to estimate their bearings in various locations.

The timestamps for the map were collected from the AIS record that was filtered for all unique timestamps for the year of 2019, West and within a cone of 60 degrees from the sensor. Bearing estimates were produced by the maximum eigengap estimator for the five minute (uncalibrated and calibrated) acoustic records associated with the unique AIS timestamps, using a frequency upper and lower bound of 100 and 300 Hz respectively. The bearing estimates were interpolated by the K-Nearest Neighbors algorithm (Pedregosa et al. 2011), using the 10 nearest neighbors. The warmer colors indicate a higher MAAD and therefore, worse performance of the maximum eigengap estimator. In the results on the uncalibrated data we see a large area due West of the 122.35 Easting which produces lower MAAD. This area is inside the shipping channel, and the lower error may be due to indirect path acoustic arrivals, or because of the increase in number of observations, or a combination of both.

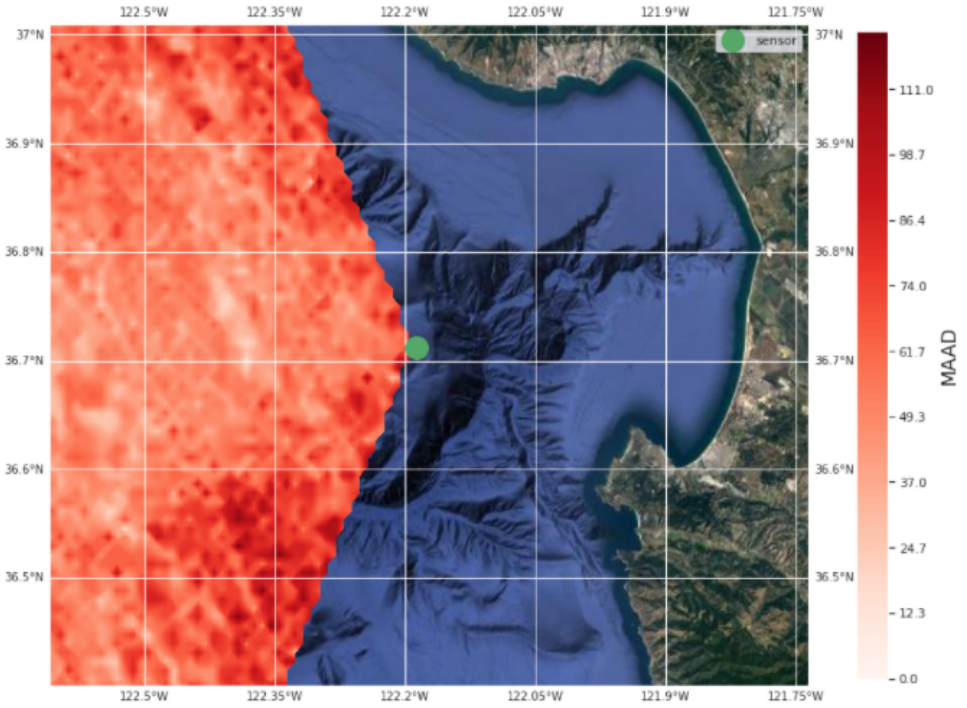

(a) Uncalibrated Vector Sensor Data

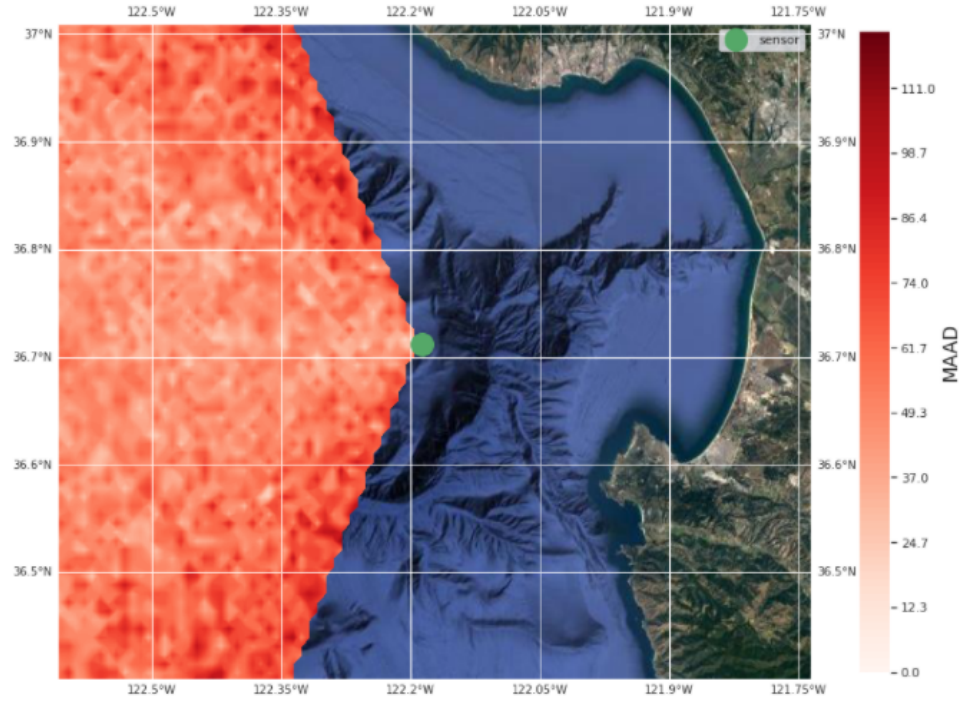

(b) Calibrated Vector Sensor Data

Figure 3.6. Map of interpolated bearing estimates.

THIS PAGE INTENTIONALLY LEFT BLANK

CHAPTER 4:
Conclusion

In this thesis we have presented the maximum eigengap estimator as a useful algorithm for performing data-driven acoustic analysis. In Chapter 1 we discussed the recent history of DOA estimation as it pertains to measurements from vector sensor's. We have applied the maximum eigengap estimator to the data discussed in Chapter 2, along with a discussion on the physical ocean environment and the results of the Bellhop ray model. The derivation presented in Chapter 3 shows the mathematical basis for the estimator. We then show the performance of the estimator through several experiments.

Figure 3.1 shows the estimator performs fairly well when the source is at a close distance (within 10 km) of the sensor. This agrees with the physical model; indicating that this is where direct path arrivals may occur. We also see in the multi-ship experiments (Figure 3.3) the estimator performs better on estimates at closer ranges. Figure 3.4 shows how well the estimator performs in direct comparison to Figures 2.5, 2.6, and 2.7. When we vary the upper and lower bounds provided to the sensor (3.5) we see the estimator performs well for a wide range of frequencies when the vessel is at a closer distance, in agreement with the intuition that transmission loss increases over distance. We also see that the estimator performs well when the frequency bounds are at low frequencies over a wide range of distances. Figure 3.6 shows the performance of the maximum eigengap estimator at scale in the form of a map of the estimator's performance. Utilization of such a map may be used to inform further scientific experiments, or for military planning efforts in the realm of vessel localization.

In summary, this thesis demonstrates that the maximum eigengap estimator is a unique and useful acoustic localization tool. It has the advantages of (1) being a data-first approach that performs automatic source frequency selection, (2) is relatively easy to scale, and (3) produces accurate estimates for direct path acoustic arrivals (where the source is within 10 km). There are significant further research opportunities to expand and explore the performance of the estimator. Some of these opportunities include analyzing the estimator's performance across various norm constraints on the optimization problem, comparing the

performance when we select AIS timestamps by season (observing the effects of a changing water column sound speed profile), and exploring other deployment environments.

List of References

Axler S (1997) *Linear algebra done right* (Springer Science & Business Media).

Berger GDH (2020) *COMMANDANT'S PLANNING GUIDANCE: 38th Commandant of the Marine Corps* (NIMBLE BOOKS).

Cadzow JA (1990) Multiple source location-the signal subspace approach. *IEEE Transactions on Acoustics, Speech, and Signal Processing* 38(7):1110–1125.

Carter GS, Gregg MC (2002) Intense, variable mixing near the head of monterey submarine canyon. *Journal of physical oceanography* 32(11):3145–3165, ISSN 0022-3670.

Etter PC (2018) *Underwater acoustic modeling and simulation* (CRC press).

GEBCO Compilation Group (2020) Gebco 2020 grid. Doi:10.5285/a29c5465-b138-234de053-6c86abc040b9.

Gemba KL, Sarkar J, Cornuelle B, Hodgkiss WS, Kuperman W (2018) Estimating relative channel impulse responses from ships of opportunity in a shallow water environment. *The Journal of the Acoustical Society of America* 144(3):1231–1244.

Hawkes M, Nehorai A (1998) Acoustic vector-sensor beamforming and capon direction estimation. *IEEE transactions on signal processing* 46(9):2291–2304.

Hollister JE (September 1975) Currents in monterey submarine canyon.

Hooijberg M (2012) *Practical Geodesy: Using Computers* (Springer Science & Business Media).

Huang Z, Xu J, Gong Z, Wang H, Yan Y (2018) Source localization using deep neural networks in a shallow water environment. *The Journal of the Acoustical Society of America* 143(5):2922–2932.

Kim W John (2020) Automating vessel detection with passive sonar signals and convolutional neural networks. URL https://calhoun.nps.edu/handle/10945/66091.

Koch RA, Knobles DP (2005) Geoacoustic inversion with ships as sources. *The Journal of the Acoustical Society of America* 117(2):626–637.

Kuhnz L, Buck K, Lovera C, Litvin S, Whaling P, Barry J (2020) Potential impacts of the monterey accelerated research system (mars) cable on the seabed and benthic faunal assemblages. *MBARI Biological Survey Report* .

Nehorai A, Paldi E (1994) Acoustic vector-sensor array processing. *IEEE Transactions on signal processing* 42(9):2481–2491.

Nichols B, Martin J, Verlinden C, Sabra KG (2019) Enhancing ambient noise correlation processing using vector sensors. *The Journal of the Acoustical Society of America* 145(6):3567–3577.

Niu H, Reeves E, Gerstoft P (2017) Source localization in an ocean waveguide using supervised machine learning. *The Journal of the Acoustical Society of America* 142(3):1176–1188.

Pedregosa F, Varoquaux G, Gramfort A, Michel V, Thirion B, Grisel O, Blondel M, Prettenhofer P, Weiss R, Dubourg V, Vanderplas J, Passos A, Cournapeau D, Brucher M, Perrot M, Duchesnay E (2011) Scikit-learn: Machine learning in python. *Journal of Machine Learning Research* 12:2825–2830.

Porter MB, Bucker HP (1987) Gaussian beam tracing for computing ocean acoustic fields. *The Journal of the Acoustical Society of America* 82(4):1349–1359.

Rockafellar RT (2015) *Convex analysis* (Princeton university press).

Rossing T (2007) *Springer handbook of acoustics* (Springer Science & Business Media).

Wainwright MJ (2019) *High-dimensional statistics: A non-asymptotic viewpoint*, volume 48 (Cambridge University Press).

Wang H, Kaveh M (1985) Coherent signal-subspace processing for the detection and estimation of angles of arrival of multiple wide-band sources. *IEEE Transactions on Acoustics, Speech, and Signal Processing* 33(4):823–831.

Zwart PB (1974) Global maximization of a convex function with linear inequality constraints. *Operations Research* 22(3):602–609.

Initial Distribution List

1. Defense Technical Information Center
   Ft. Belvoir, Virginia

2. Dudley Knox Library
   Naval Postgraduate School
   Monterey, California